MODELLING OF THERMAL ENERGY STORAGE SYSTEMS FOR BULK ELECTRICITY STORAGE

FIRST YEAR REPORT

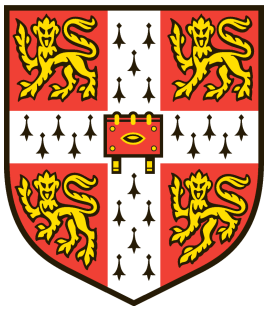

Pau Farrés Antúnez

CAMBRIDGE UNIVERSITY

ENGINEERING DEPARTMENT

-DIVISION A-

28th August 2015

This report has been submitted for the First Year Assessment of the PhD course in Engineering at Cambridge University Engineering Department.

Author:	Pau Farrés Antúnez (P. Farres-Antunez)
	pf298@cam.ac.uk
Supervisor:	Dr. Alex White
College:	Peterhouse
Date:	28th August 2015

Contents

Abstract

Growing concerns about climate change and energy security are increasing worldwide efforts to decarbonize the electrical grids, pushing governments and international institutions to promote the use of Renewable Energies (RE). However, two major RE sources -wind and solar energy- present natural fluctuations, and any grid containing big portions of such sources faces the major challenge of having enough electricity storage available to match supply and demand. A new family of technologies with a high potential for large-scale electricity storage applications is emerging, which in this report are denominated Thermo-Electrical Energy Storage (TEES) systems. Generally, in a TEES system, a heat pump uses electricity to transport thermal energy from one thermal reservoir (cold) into another (hot). Energy may be stored in the form of sensible or latent heat. After storage, a heat engine is used to transform the thermal energy back into electricity. Differently from the two main competing technologies -Pumped Hydro-electric Storage (PHS) and Compressed Air Energy Storage (CAES)-, the implementation of a TEES system does not depend on specific geographical features. Additionally, it normally makes use of cheap and abundant materials and benefits from high values of energy density.

The aim of this PhD project is the analysis and comparison of TEES cycles through component and cycle modelling, the identification of their main strengths and weaknesses and the suggestion of novel configurations with improved performance.

The first part of this report is mainly concerned with the thermodynamic analysis of a specific TEES technology which is based on the Joule-Brayton (JB) cycle and is known as Pumped Thermal Electricity Storage. Chapter 2 reviews the fundamentals of the technology and proposes and evaluates new configurations that make use of liquid materials as storage media, substituting the solid reservoirs that have been used until now. It also presents and briefly discusses other TEES technologies that are based on variations of the Rankine cycle.

The second part of this report, Chapter 3, is concerned with the modelling of specific components used in TEES cycles, such as a heat exchanger or a reciprocating compressor, and the study of packed-beds of solid particles for thermal energy storage using Computational Fluid Dynamics (CFD).

Finally, a summary of the work done up-to-date and the proposed work for the continuation of the project is presented.

Nomenclature

Acronyms

BDC, TDC	Bottom Dead Centre, Top Dead Centre
CAES	Compressed Air Energy Storage
CFD	Computational Fluid Dynamics
CUED	Cambridge University Engineering Department
CSP	Concentrated Solar Power
JB	Joule-Brayton (cycle)
OpenFOAM	Open-source Field Operation And Manipulation (software)
PCM	Phase Change Material
PHS	Pumped Hydro energy Storage
PTES	Pumped Thermal Energy Storage
RANS	Reynolds-Averaged Navier Stokes equations
SEGS	Solar Energy Generating System
SHE	Screw Heat Exchanger
TES	Thermal Energy Storage
TEES	Thermo-Electrical Energy Storage

Latin symbols

A	Area [m^2]
b	Empirical coefficient (as defined in Equation 3.6) [m^{-1}]
CA	Crank Angle [$^\circ$]

COP	Coefficient of Performance [-]
C_d	Drag coefficient (see equation (3.2)) [-]
c_p	Isobaric specific heat capacity [$\mathrm{J/(kg\,K)}$]
c_s	Specific heat capacity (solid) [$\mathrm{J/(kg\,K)}$]
c_v	Isochoric specific heat capacity [$\mathrm{J/(kg\,K)}$]
d	Total derivative [-]
∂	Partial derivative [-]
d_c, d_p	Cylinder diameter, particle diameter [m]
F	Total pressure loss factor (see Equation (2.22)) [-]
F_d, F_p, F_μ	Drag force, pressure force, force due to viscous shear stress [N]
h	Specific enthalpy (except in section 3.4) [$\mathrm{J/kg}$]
h	Heat transfer coefficient (only in section 3.4) [$\mathrm{W/(m^2\,K)}$]
int()	Integral [-]
K	Permeability coefficient (as defined in Equation 3.6) [$\mathrm{m^2}$]
m	Mass [kg]
n	Number of expansions (as described in section 2.3.2.2) [-]
Nu	Nusselt number (see Equation (3.3)) [-]
p	Pressure [Pa]
p_ρ	Kinematic pressure [$\mathrm{m^2/s^2}$]
Q	Heat transfer [J]
$\dot{q}$	Heat transfer rate [W]
Re	Reynolds number (see Equation (3.1)) [-]
t	Time [s]
T	Temperature [K]
u	Velocity [$\mathrm{m/s}$]
U	Overall heat transfer coefficient [$\mathrm{W/(m^2\,K)}$]
x	Space coordinate [m]

w, w_x	Specific work, specific work output [J/kg]

Greek symbols

α	Thermal diffusivity [m^2/s]
β	Pressure ratio [-]
δ	Infinitesimal increment [-]
Δ	Finite increment [-]
ε	Void fraction [-]
η	Efficiency [-]
γ	Heat capacity ratio [-]
κ	Thermal conductivity [W/m K]
μ	Dynamic viscosity [Pa s]
∇	Nabla operator [m^{-1}]
ν	Kinematic viscosity [m^2/s]
ϕ	Polytropic index (see Equations (2.6) and (2.7)) [-]
ρ	Mass density [kg/m^3]
ρ_E	Energy density [J/m^3]
τ	Temperature ratio, $\tau \equiv T_1/T_2$ [-]
θ	Temperature ratio, $\theta \equiv T_3/T_1$ (except in section 3.4) [-]
θ	Angular position around a cylinder (only in section 3.4) [°]
χ	Maximum round-trip efficiency [-]

Subscripts

c, e	Compressor, expander
ch, dis	Charge, discharge
CS, HS	Cold store, hot store
eff	Effective

g, l, s	Gas, liquid, solid
h, c	Hot, cold
HP, HE	Heat pump, heat engine
i	Each of the three components in Cartesian coordinates, x, y and z.
in, out	Inlet, outlet
min, max	Minimum, maximum
net	Net
rev	Reversible process

Superscripts

∞	Free-stream conditions
$\prime$	Discharge
$\rightarrow$	Vector

Chapter 1

Introduction

1.1 The need for bulk electrical energy storage. Main technologies and applications

Global awareness on the intrinsic problems of a fossil-fuel-based energy system is emerging. Climate change, among many other economic, environmental, social and political reasons -such as the increasing price of fossil fuels, high levels of pollution, and concerns for energy security due to resource depletion and dependence on politically unstable regions- are driving new policies in Europe and world-wide that promote the use of Renewable Energies (RE) as sustainable and carbon-free sources of energy. A good example of this is the 2009 EU Renewables Directive, which established mandatory national targets to achieve that 20 % of the communitarian energy consumption comes from renewable sources by 2020 [1].

Nevertheless, increasing portions of wind and solar energy in the electrical grid involves large fluctuations in electrical supply that complicates matching the demand. Several strategies are being considered to mitigate the extent of the problem -such as power grid interconnection and trading within large geographical areas with distributed RE sources, thereby cancelling regional variations, or smart grids and loads that can adapt or postpone demand according to conditions in the supply side-, although, eventually, an amount of large-scale energy storage becomes a necessary piece of the puzzle [2].

In a rough but illuminating example, MacKay estimates that supplying 20% of the UK's electricity consumption with wind power would require an accumulated storage capacity of 1200 GWh to compensate for a generalised wind lull that lasted for up to 5 days [3]. In contrast, all current Pumped Hydro-electric Storage (PHS) facilities in the UK add up to less than 30 GWh, while most of the suitable places to install new plants are already in use. Similar conclusions are drawn by Wilson et al., who indicate that the decarbonization challenge cannot be solved independently from the energy storage challenge [4].

A number of different energy storage technologies are available, each having a preferred range of application. For example, flywheels, batteries, capacitors and super-capacitors are mostly suited for *power quality* and (short-duration) uninterrupted power supply [5]. In the present work, however, we are concerned with technologies suited for *energy management*, and particularly in the large-scale. For small/medium-scale energy management ($\sim 1-100\,\mathrm{MW}$), flow batteries, large-scale conventional batteries, fuel cells and solar fuels may be used [6]. For large-scale energy management (above 100 MW), on the other hand, the best suited technologies are PHS, Compressed Air Energy Storage (CAES) and Thermal Energy Storage (TES), as they present good scalable characteristics and a comparatively low price per unit of stored energy. PHS is the most mature technology and benefits from long lifetimes and high round-trip efficiencies (above 70 %). While traditional CAES makes use of fossil fuels to run the discharge cycle, the less mature Advanced-Adiabatic CAES is strictly a storage system and may achieve efficiencies comparable to PHS systems [7]. Nevertheless, the implementation of both PHS and CAES depends on favourable geographic features (ability to construct large water reservoirs at different heights in the first case, existence of large underground caverns in the second), while TES systems do not suffer from such constraints and typically present higher energy densities.

TES systems may be broadly classified according to the nature of their energy input and output, which may be either thermal energy or electricity:

Energy Input	**Energy Output**	**Application example**
Thermal	Thermal	Solar water heating
Thermal	Electrical	Concentrated Solar Power plants
Electrical	Thermal	Heat pumps and refrigerators
Electrical	Electrical	Large-scale electricity storage

In the present report, attention will be placed on the last group of TES technologies, which store electricity in the form of thermal energy and may be named Thermo-Electrical Energy Storage (TEES) systems.

1.2 Thermal Energy Storage for electricity storage

1.2.1 Basic principles

TEES technologies store electricity in the form of thermal energy. The basic principle of such systems is presented in Figure 1.1. During charge, an electric motor is used to drive a heat pump which transforms mechanical work into a thermal potential, transporting heat

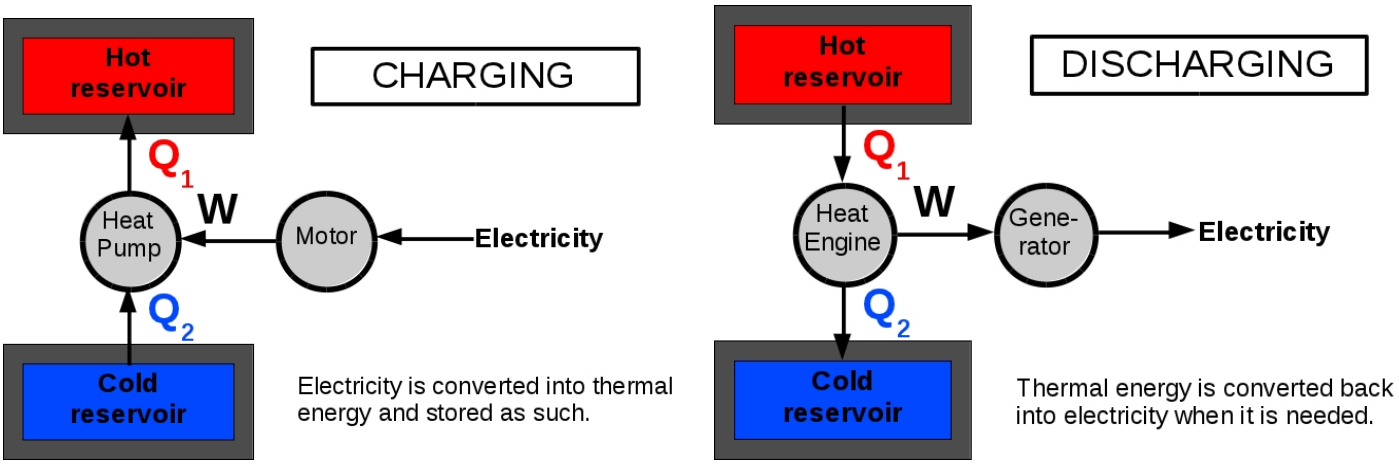

Figure 1.1: Generic representation of an electrically-driven heat pump and heat engine system with two thermal reservoirs for electricity storage.

from a cold reservoir into a hot reservoir. The thermal energy is stored in the form of either sensible heat or latent heat, and the reservoirs are fully insulated to minimize thermal losses during the storage period. When electricity is needed, a heat engine drives heat from the hot reservoir back into the cold reservoir, extracting useful work that is transformed into electricity via a generator.

Although several irreversible processes exist that negatively affect the performance of any real TEES system, the ideal round-trip efficiency of such a cycle is one. This is because the Coefficient Of Performance (COP) of a *reversible* heat pump operating between two reservoirs (one at temperature T_h and the other at T_c) is equal to 1 over the efficiency of an also reversible heat engine operating between the same temperatures. Mathematically, the round-trip efficiency of such a reversible compound system is:

$$\chi_{rev} = COP_{HP,rev} \cdot \eta_{HE,rev} = \left(\frac{T_h}{T_h - T_c}\right) \cdot \left(\frac{T_h - T_c}{T_h}\right) = 1$$

1.2.2 TEES technologies under development

Several energy storage technologies that are based on the principle just presented have been proposed during the last few years or decades:

- Cryogenic Energy Storage (CES), also known as Liquid Air Energy Storage (LAES), uses electricity to refrigerate and liquefy air. Liquid air is stored as such and is used to generate electricity when needed. The high energy and power densities are two key points of this technology, which, on the other hand, currently suffers from a low round-trip-efficiency ($\lesssim 50\,\%$) due to the high energy consumption used for air liquefaction [5].

- A TEES system based on the transcritical CO_2 cycle has been recently suggested which uses ice as the cold reservoir and hot water as the hot reservoir. Two versions of the system have been presented, with one system using an adiabatic expansion during discharge while the other one using an isothermal expansion [8]. A similar system based on the ammonia cycle has been suggested, which uses solar thermal panels to enhance its round-trip-efficiency [9]. Both technologies benefit from a high work ratio between expander and compressor and make use of water as cheap and abundant storage media. On the other hand, the relatively small temperature difference between the two thermal reservoirs poses strong requirements on the maximum finite temperature difference which may be allowed during the heat transfer processes with both reservoirs if the round-trip efficiency is to be kept high (see section 2.2.8 for a discussion on this topic).

- Pumped Thermal Electricity Storage, which is based on the Joule-Brayton (JB) cycle and stores sensible heat in solid reservoirs, has received attention during the recent years by our research group at Cambridge University Engineering Department (CUED) and is a main focus of this report. Chapter 2 will present this technology in depth, apart from suggesting and evaluating new potential configurations that make use of liquid storage media.

1.3 Goals of this project

The first aim of the proposed PhD project is the study and comparison between solid TES and liquid TES systems from the perspective of exergy conservation maximization. To do so, solid packed-bed thermal reservoirs are being studied using CFD tools, and a 1D model of a heat exchanger for liquid thermal reservoirs is being developed (see Chapter 3 for more details).

The second aim is the analysis, simulation and comparison of complete TEES cycles, the identification of their main strengths and weaknesses and the suggestion of novel configurations with improved performance and viability for large-scale electricity storage applications (see Chapter 2).

Chapter 2

Thermodynamic cycle analysis

2.1 Goals and methods

The aim of this chapter is to evaluate the thermodynamic performance of different thermal energy storage cycles for bulk electricity storage using simple analytical tools. The focus on sections 2.2 and 2.3 is on different configurations of the Joule-Brayton (JB) cycle, while section 2.4 discusses different schemes based on the Rankine cycle.

The analysis presented in section 2.2 has been mainly based on, and expanded from, those presented in [10, 11, 12, 13]. Apart from setting important fundamentals that will be useful during the rest of the report, the section calls attention onto some aspects that were not discussed in the mentioned articles, such as the impact of varying the pressure ratio when the maximum temperature of the system is fixed. Section 2.3, on the other hand, presents and evaluates the feasibility of new adaptations of the JB cycle for electricity storage that make use of liquid media and are fully original from this report. Finally, section 2.4 will both review Rankine-based schemes presented in the literature and suggest new routes for improvement.

2.2 The Joule-Brayton cycle for electricity storage

2.2.1 Previous work

Using the Joule-Brayton (JB) cycle for electricity storage purposes is a novel technology that initiated its development over the last decade. It is often denominated Pumped Thermal Electricity Storage (PTES). This and other similar technologies based on other thermodynamic cycles may be also called Thermo-Electrical Energy Storage (TEES) systems. Two different PTES concepts based on the same underlying principles were independently patented

in 2007 by Ruer [14] and by Macnaghten and Howes [15]. Although with some variations, both systems use the JB cycle and are based on the idea of using a heat pump to transform electricity into thermal energy, store it into two fully insulated tanks (one hot, one cold, filled with a solid medium with high specific heat capacity), and then reverse the cycle, operating the heat pump as a heat engine to transform the thermal energy back into electricity.

The first scientific publication appeared in 2010 from Desrues et al. [12], followed by various publications from White and McTigue et al. [11, 16, 17, 18] between 2011 and 2015. These mainly present thermodynamic analysis and computational models to provide a better understanding of the general behaviour of the system and how the various sources of loss affect its performance. Finally, in 2012, building on the concept patented in [15], Howes provided a more practical perspective with an article that describes experimental tests being run by Isentropic Ltd., aimed at constructing the first pilot "Pumped Heat Energy Storage" system [19].

In the following sections the principles of the JB-based PTES will be presented, as well as the few conceptual differences between the systems suggested in [12] and in [15].

2.2.2 Main components and stages

The layout of a JB-based PTES system is presented in Figure 2.1, together with a T-s diagram of the ideal cycle. The following components may be identified:

Compressor/expander (C/E): Which can be turbomachines (as in [12]) or reciprocating devices (as in [15]). They exchange energy with the grid via an electrical motor (charge) or generator (discharge), and drive the working fluid around the cycle. The working fluid may be air or argon. The higher heat capacity ratio of argon ($\gamma = c_p/c_v$) has the advantage of requiring lower pressure ratios for a given temperature ratio.

Hot and cold thermal stores (HS/CS): Filled with a solid media with high specific heat capacity which can be cycled over the selected temperature range without deterioration. This could be in the form of a matrix of refractory material (as in [12]) or as a packed bed of solid particles (as in [15]). In the diagram presented in Figure 2.1, the two thermal tanks are assumed to be at ambient temperature when discharged.

Heat exchangers (HX1/HX2): Which are used to reject waste heat to the environment. As the real cycle contains several sources of irreversibility, the discharge cycle is not able to recover all the energy injected during charge and waste heat needs to be rejected.

During charge, the compressor receives power from an electric motor and brings the gas from atmospheric conditions (point 1 in Figure 2.1) to a higher temperature and pressure (point 2); ideally, this is an adiabatic and reversible (therefore isentropic) compression.

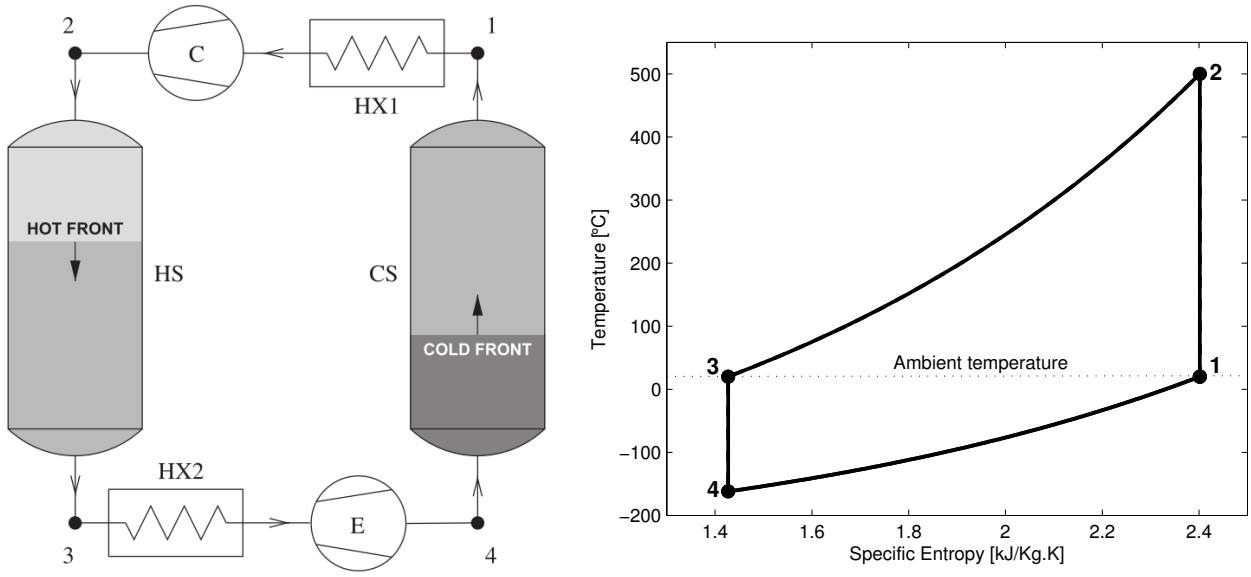

Figure 2.1: Left: Simplified layout of a PTES system, from [17]. Right: T-s diagram corresponding to the ideal cycle.

The gas entering the hot thermal store exchanges heat with the solid medium, thereby cooling down at approximately constant pressure. This generates a thermal front that advances through the tank as the charging process continues. The gas leaves the hot tank at ambient temperature and high pressure (point 3) and enters the expander, where it does work, partially compensating for the compressor power input, while bringing the gas back to ambient pressure and at a lower temperature (point 4). Ideally, the expansion would be isentropic. Finally, the gas enters the cold store, where it will be brought back to ambient temperature (point 1) while cooling down the solid media inside the tank, generating again a thermal front that advances through the tank. Overall, the system receives power from an external source (the electrical grid) and behaves as a heat pump, transporting heat from the cold tank to the hot tank.

During discharge, the direction of the flow is reversed and the expander is replaced by a compressor, and vice versa. The system behaves as a heat engine, transporting heat from the hot tank to the cold tank while generating power that is injected back to the grid.

2.2.3 Energy density

The nominal energy density of the system, ρ_E, may be defined as the maximum net energy stored during charge over the total volume of the solid media from both the hot and the cold thermal stores. The net energy input has to be equal to the increase in thermal energy of the hot and cold stores: $E_{net} = \Delta E_{HS} + \Delta E_{CS}$. Additionally, $V_{HS} = {}^{m_{HS}}/_{\rho_s}$ and $V_{CS} = {}^{m_{CS}}/_{\rho_s}$. Therefore, in the limit where both stores are completely charged:

$$\rho_E = \frac{E_{net}}{V_{HS} + V_{CS}} = \frac{\rho_s \left(\Delta E_{HS} + \Delta E_{CS}\right)}{m_{HS} + m_{CS}} = \frac{\rho_s \left[m_{HS} c_{HS} \left(T_2 - T_3\right) + m_{CS} c_{CS} \left(T_4 - T_1\right)\right]}{m_{HS} + m_{CS}} \quad (2.1)$$

Note that the right hand side of Equation (2.1) is only valid if the specific heat capacities of the storage media are constant or if c_{HS} and c_{CS} represent *average* values over the relevant temperature ranges. Within each reservoir, the temperature variation experienced by the storage media during the heat transfer process is the exact opposite than the one experienced by the gas. This allows us to write $m_{HS} c_{HS} = \left[m_g c_{p,g}\right]_{HS}$ and $m_{CS} c_{CS} = \left[m_g c_{p,g}\right]_{CS}$. Knowing that the same mass of gas is circulated through both reservoirs, and assuming the gas may be treated as a perfect gas (i.e. with constant $c_{p,g}$), we can write $m_{HS} c_{HS} = m_{CS} c_{CS}$. In reality, the big temperature difference between the two reservoirs means that $c_{CS} < c_{HS}$ (assuming the storage media is the same) and therefore $m_{CS} > m_{HS}$. Nevertheless, it is sometimes useful to assume that $c_{CS} = c_{HS} \equiv c_s$ and $m_{CS} = m_{HS} \equiv m_s$ for illustrative purposes, to obtain a quick (and rough) approximation, in which case Equation (2.1) can be expressed as:

$$\rho_E = \frac{\rho_s \left[m_s c_s \left(T_2 - T_3\right) + m_s c_s \left(T_4 - T_1\right)\right]}{2 m_s} = \frac{1}{2} \rho_s c_s \left[\left(T_2 - T_3\right) - \left(T_1 - T_4\right)\right] \quad (2.2)$$

2.2.4 Adiabatic compression and expansion work

In this section, it will be assumed that the compression and expansion stages occur fast enough to be adiabatic. This is considered an accurate approximation for turbomachine devices, where the flow speeds are high, and will be accurate for reciprocating devices as long as they are insulated. If kinetic energy and potential terms are also ignored, the Steady Flow Energy Equation simplifies to:

$$w_x = -\Delta h$$

where w_x represents specific work output and Δh the increase of specific enthalpy between the inlet and outlet of the compressor or expander. Assuming perfect gas behaviour (which will be accurate if the working fluid is argon, but may not be so accurate at high temperatures if the working fluid is air), the increase in specific enthalpy becomes

$$\Delta h = c_p \Delta T = c_p \left(T_{out} - T_{in}\right)$$

In the case of a compressor, the work transfer is a work *input*, i.e. $w_c = -w_x$, while for the expander it is a work *output*, $w_e = w_x$. This allows to write:

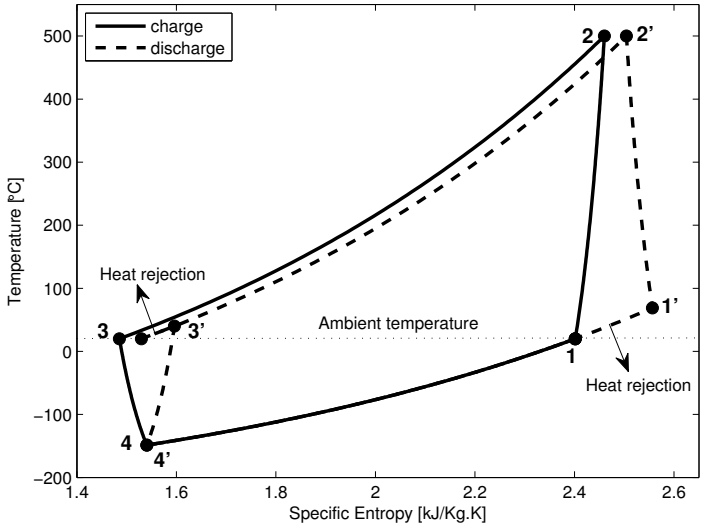

Figure 2.2: T-s diagram showing a non-ideal Joule-Brayton cycle during charge (1-2-3-4-1) and discharge (1-4′-3′-2′-1′).

$$w_c = c_p \left(T_{out} - T_{in}\right)$$
$$w_e = c_p \left(T_{in} - T_{out}\right)$$

From this point, the expressions of net input and output work of the Joule-Brayton cycle during charge and discharge can be obtained by reference to Figure 2.2, which shows the reference points during a non-ideal charge (1-2-3-4-1) and discharge (1-4′-3′-2′-1′). An arbitrary value of the polytropic efficiency of 0.94 has been used for the compression and expansion stages to generate the diagram. Notice that during the discharge cycle heat rejection to the environment becomes necessary to restore the initial conditions. In the case of the diagram in Figure 2.2 (and with reference to the PTES layout presented in Figure 2.1) this is done by operating the two heat exchangers, HX1 and HX2, between $T_{1'}$ and T_1 and between $T_{3'}$ and T_3, respectively. In this case, both T_1 and T_3 are set to ambient temperature.

During charge, the specific net work *input* will be:

$$w_{net,ch} = w_c - w_e = c_p \left(T_2 - T_1\right) - c_p \left(T_3 - T_4\right) \tag{2.3}$$

During discharge (denoted by ′), the specific net work *output* will be:

$$w_{net,dis} = w'_e - w'_c = c_p \left(T_{2'} - T_{1'}\right) - c_p \left(T_{3'} - T_{4'}\right) \tag{2.4}$$

2.2.5 Pressure and temperature polytropic relationships

The *isentropic* efficiency of a compressor or expander varies with the pressure ratio, and it could be misleading when comparing the efficiencies of two processes that operate at different pressure ratios [20]. Since we will be interested on analysing the impact of operating the PTES system at different temperature and pressure conditions, it is more adequate to use the *polytropic* efficiency. For a compressor, it is defined as the ratio between the reversible work input and the actual work input for an infinitesimal compression process, as follows:

$$\eta_c \equiv \frac{\delta w_{c,rev}}{\delta w_c}$$

The reversible work input of an infinitesimal compression is $\delta w_{c,rev} = {}^{dp}/_{\rho}$ [10]; this can be derived from the steady flow energy equation (neglecting the kinetic and potential terms), the "TdS" equation for the enthalpy, $Tds = dh - {}^{dp}/_{\rho}$, and the expression of entropy change for a steady and reversible flow in an infinitesimal control volume, $ds = {}^{dq}/_{T}$. If the actual process is adiabatic and the fluid is a perfect gas, we can write $\delta w_c = dh = c_p dT$. Therefore,

$$\eta_c = \frac{{}^{dp}/_{\rho}}{c_p dT} \tag{2.5}$$

Using the ideal gas equation, $\rho = {}^{p}/_{RT}$, and integrating, a relationship is obtained between the pressure and the temperature for a polytropic compression:

$$\begin{gathered} \frac{T_{out}}{T_{in}} = \left(\frac{p_{out}}{p_{in}}\right)^{\phi_c} \\ \phi_c \equiv \frac{\gamma-1}{\eta_c \gamma} \end{gathered} \tag{2.6}$$

Reproducing this same analysis for an expander leads to:

$$\eta_e = \frac{c_p dT}{{}^{dp}/_{\rho}}$$

$$\begin{gathered} \frac{T_{out}}{T_{in}} = \left(\frac{p_{out}}{p_{in}}\right)^{\phi_e} \\ \phi_e \equiv \frac{\eta_e(\gamma-1)}{\gamma} \end{gathered} \tag{2.7}$$

Defining β as the pressure ratio for a compression/expansion and τ as the corresponding temperature ratio, we can similarly write:

$$\begin{gathered} \tau_c = \beta_c^{\phi_c} \\ \tau_e = \beta_e^{\phi_e} \end{gathered} \tag{2.8}$$

2.2.6 Impact of polytropic efficiency on the cycle's round-trip-efficiency and energy density

The cycle's round-trip-efficiency eventually depends on the coupled behaviour of a rather big number of factors, such as the different loss processes at each component of the cycle. Additionally, the development of thermal fronts generated inside the thermal storage tanks is an unsteady process and the amount of energy that can be finally recovered depends on the history of the charging, storage, and discharging stages. This hysteresis, together with the temperature dependence of the materials' thermophysical properties, make an accurate hand analysis of the system performance impossible. Numerical computation becomes necessary instead in order to obtain predictions that are realistic enough. Nevertheless, some approximations can still be made that enable us to proceed analytically and provide very useful information on the general trends of the system. For instance, we can obtain an upper-limit of the round-trip efficiency by assuming that PTES system is globally adiabatic and neglecting the hysteresis processes in the reservoirs; in other words, we are assuming that during discharge we are able to deplete all the energy that was stored during charge (converting part of it into useful work and rejecting another part to the environment through the heat exchangers). If we do so, then we can express the round-trip efficiency simply as the fraction between the net specific work during discharge over the net specific work during charge:

$$\chi = \frac{w_{net,dis}}{w_{net,ch}} = \frac{(T_{2'} - T_{1'}) - (T_{3'} - T_{4'})}{(T_2 - T_1) - (T_3 - T_4)} \tag{2.9}$$

where equations (2.3) and (2.4) have been used. Note again that the temperature points are taken with reference to Figure 2.2 and that the equations consider that the working fluid behaves as a perfect gas. Also note that, neglecting thermal losses between the charge and the discharge period, the outlet temperature of each thermal tank during discharge will be the same as its inlet temperature during charge, i.e. $T_{2'} = T_2$ and $T_{4'} = T_4$.

Let us define τ as the compressor's temperature ratio during charge, $\tau \equiv \tau_c = {}^{T_2}/_{T_1}$. The expander's temperature ratio is $\tau_e = {}^{T_3}/_{T_4}$. For the discharge cycle, we have $\tau' \equiv \tau'_e = {}^{T_{2'}}/_{T_{1'}}$ and $\tau'_c = {}^{T_{3'}}/_{T_{4'}}$. Equation (2.9) can be rewritten:

$$\chi = \frac{w_{net,dis}}{w_{net,ch}} = \frac{T_{1'}\,(\tau' - 1) - T_{3'}\,(1 - {}^1/_{\tau'_c})}{T_1\,(\tau - 1) - T_3\,(1 - {}^1/_{\tau_e})} \tag{2.10}$$

Neglecting pressure losses for the moment, the pressure ratio over the expander has to be the same than over the compressor: $\beta_e = \beta_c$. According to (2.8) this implies $\tau_e^{1/\phi_e} = \tau_c^{1/\phi_c}$. Therefore:

$$\tau_e = \tau_c^{\phi_e/\phi_c} = \tau^{\phi_e/\phi_c} = \tau^{\eta_e \eta_c}$$

Repeating the same argument for the discharge cycle and assuming for simplicity that the compressors and the expanders have the same polytropic efficiency, $\eta_e = \eta_c \equiv \eta$, we obtain:

$$\begin{aligned} \tau_e = \tau^{\eta^2} \quad &\Rightarrow \quad {}^{T_3}/_{T_4} = \left({}^{T_2}/_{T_1}\right)^{\eta^2} \\ \tau_c' = \tau'^{1/\eta^2} \quad &\Rightarrow \quad {}^{T_{3'}}/_{T_{4'}} = \left({}^{T_{2'}}/_{T_{1'}}\right)^{\eta^2} \end{aligned} \tag{2.11}$$

The maximum round-trip efficiency becomes:

$$\chi = \frac{T_{1'}\left(\tau' - 1\right) - T_{3'}\left(1 - \tau'^{-1/\eta^2}\right)}{T_1\left(\tau - 1\right) - T_3\left(1 - \tau^{-\eta^2}\right)} \tag{2.12}$$

Multiplying by ${}^{T_1}/_{T_1}$ and defining a new temperature ratio $\theta \equiv {}^{T_3}/_{T_1}$:

$$\chi = \frac{{}^{\tau}/_{\tau'}\left(\tau' - 1\right) - {}^{T_{3'}}/_{T_1}\left(1 - \tau'^{-1/\eta^2}\right)}{\left(\tau - 1\right) - \theta\left(1 - \tau^{-\eta^2}\right)} \tag{2.13}$$

Where $T_{2'} = T_2$ has been used to turn ${}^{T_{1'}}/_{T_1}$ into ${}^{\tau}/_{\tau'}$. Finally, using (2.11) and $T_{4'} = T_4$ we find that ${}^{T_{3'}}/_{T_1} = \theta\tau'^{1/\eta^2}\tau^{-\eta^2}$. Substituting and rearranging,

$$\chi = \frac{\tau\left(1 - {}^{1}/_{\tau'}\right) - \theta\tau^{-\eta^2}\left(\tau'^{1/\eta^2} - 1\right)}{\left(\tau - 1\right) - \theta\left(1 - \tau^{-\eta^2}\right)} \tag{2.14}$$

Reached this point, it is important to realize that χ depends on three *operating* parameters, the charge temperature ratio τ (related to the charge pressure ratio), the discharge temperature ratio τ' (related to the discharge pressure ratio), and the ratio between T_3 and T_1, θ. Note that T_3 and T_1 are the temperatures at which the reservoirs stay when discharged. The minimum value of τ' will normally be the one which ensures that $T_{3'} = T_3$, as in the left part of Figure 2.3, where the discharge compressor operates at the exact pressure ratio that ensures that its outlet is at the same temperature than the inlet temperature of the hot reservoir. In that case, all the heat will be rejected through the first heat exchanger, HX1, between $T_{1'}$ and T_1 (which in this case is at ambient temperature). For $T_{3'}$ to be equal to T_3, the temperature ratio over the discharge compressor must be the same as the temperature ratio over the charge expander, i.e. $\tau_c' = \tau_e$. Using the relationships in 2.11, this implies that , $\tau_{min}'^{1/\eta^2} = \tau^{\eta^2}$ or:

$$\tau_{min}' = \tau^{\eta^4} \tag{2.15}$$

On the other hand, the maximum value of τ' is given by the discharge pressure ratio that

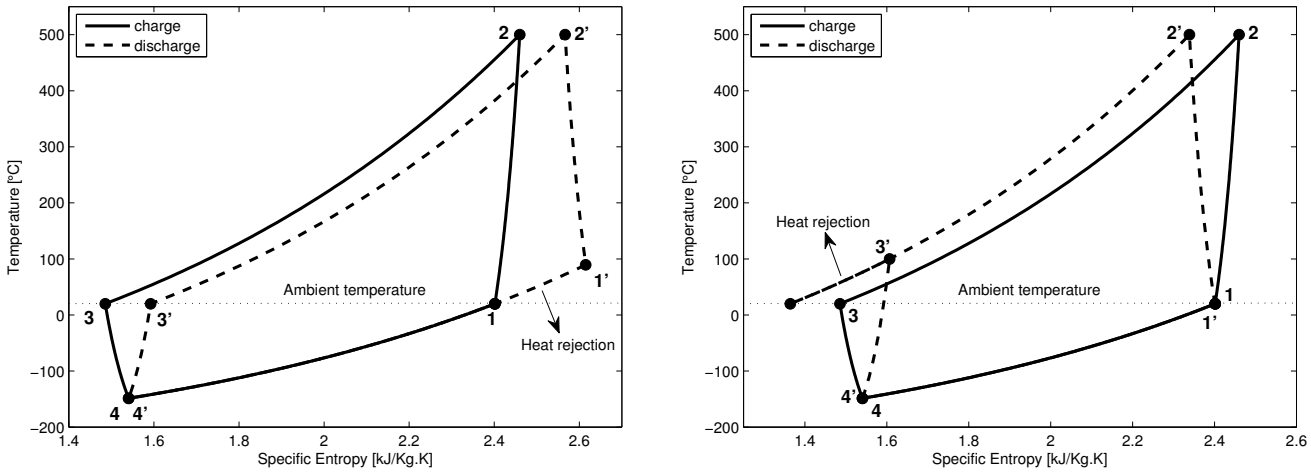

Figure 2.3: Left: T-s diagram showing the minimum discharge pressure ratio, with all heat rejection through HX1. Right: T-s diagram showing the maximum discharge pressure ratio, with all heat rejection through HX2. The optimal value, in terms of round-trip efficiency, lies somewhere in between.

forces all the heat to be rejected through the second heat exchanger, HX2, between $T_{3'}$ and T_3 (which in this case is also at ambient temperature), as in the right hand side of Figure 2.3. We have $T_{1'} = T_1$ and $T_{2'} = T_2$:

$$\tau'_{max} = \tau \tag{2.16}$$

An interesting aspect which is not shown in the main articles that describe the fundamentals of PTES (such as [11, 12]) is the impact on the maximum round-trip efficiency, χ, of varying the discharge temperature ratio, τ', with respect to the charge temperature ratio. This is shown in the left hand side of Figure 2.4. The minimum and maximum values of τ' have been set according to (2.15) and (2.16). In the figure, we can see that χ rapidly increases with lowering θ. This is because the temperatures at which the charge compressor operates are higher (as shown in the right hand side of the same figure for $\tau' = \tau = 2.5$ and $\theta = 0.7$), which increases the net specific work and reduces the negative effect of low polytropic efficiencies. It should also be noticed that for $\theta = 1$ the optimal value of τ' is almost equal to τ'_{min}, and the best strategy in this case would be to only reject heat through HX1. On the other hand, as soon as θ starts decreasing the optimal τ' rapidly shifts to higher values, much closer to τ'_{max}, and in this case the best strategy would be to use either both heat exchangers or only HX2.

The analyses of the JB cycle presented in [10, 11] show, among other things, the impact of pressure losses and polytropic efficiencies on the round-trip efficiency as a function of τ and θ. This is interesting because the cost of the hot thermal tank will increase considerably

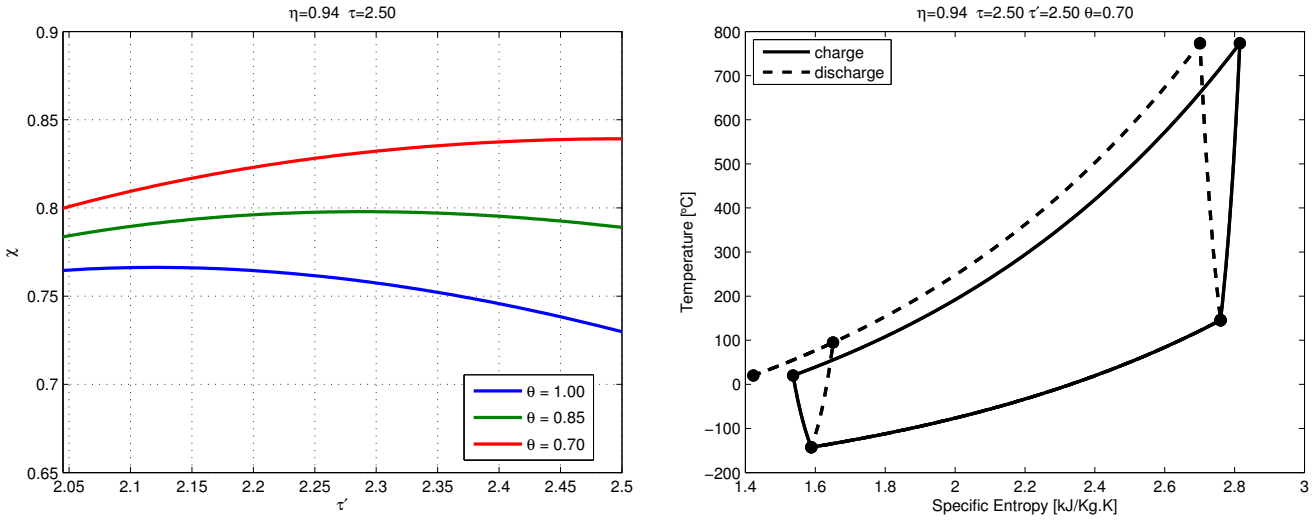

Figure 2.4: Left: Plot of the maximum round-trip efficiency, χ, as a function of the discharge temperature ratio, τ', for fixed values of η and τ and three values of θ. Right: T-s diagram corresponding to $\eta = 0.94$, $\tau = 2.5$ and $\theta = 0.70$.

with the pressure that it will need to withstand, which only depends on τ. Nevertheless, another important factor that is not being explicitly considered in those analyses is the maximum system temperature, T_2. T_2 grows both with τ and θ and will be limited by material constraints, such as the maximum temperature at which the charge compressor can operate. It is therefore interesting to rewrite the expression of χ as a function of τ, T_2 and T_3 instead, where T_3 is fixed at ambient temperature. Multiplying 2.14 by T_1/T_1 we obtain:

$$\chi = \frac{T_2\left(1 - 1/\tau'\right) - T_3\tau^{-\eta^2}\left(\tau'^{1/\eta^2} - 1\right)}{T_2\left(1 - 1/\tau\right) - T_3\left(1 - \tau^{-\eta^2}\right)} \tag{2.17}$$

Further assuming that we operate it at $\tau' = \tau'_{max} = \tau$:

$$\chi = \frac{T_2\left(1 - 1/\tau\right) - T_3\tau^{-\eta^2}\left(\tau^{1/\eta^2} - 1\right)}{T_2\left(1 - 1/\tau\right) - T_3\left(1 - \tau^{-\eta^2}\right)} \tag{2.18}$$

At this point it is important to realize that, when T_2 and T_3 are fixed, χ becomes a *decreasing* function with τ, contrary to what was found before in Equation (2.14), where T_2 was allowed to increase both with τ and θ. The same is not true for the energy density, however. A more useful definition of the energy density than that given by Equation (2.2) can be obtained by considering the same volume but only the energy that can actually be recovered, i.e. the *discharge* energy density, ρ'_E. By definition of χ:

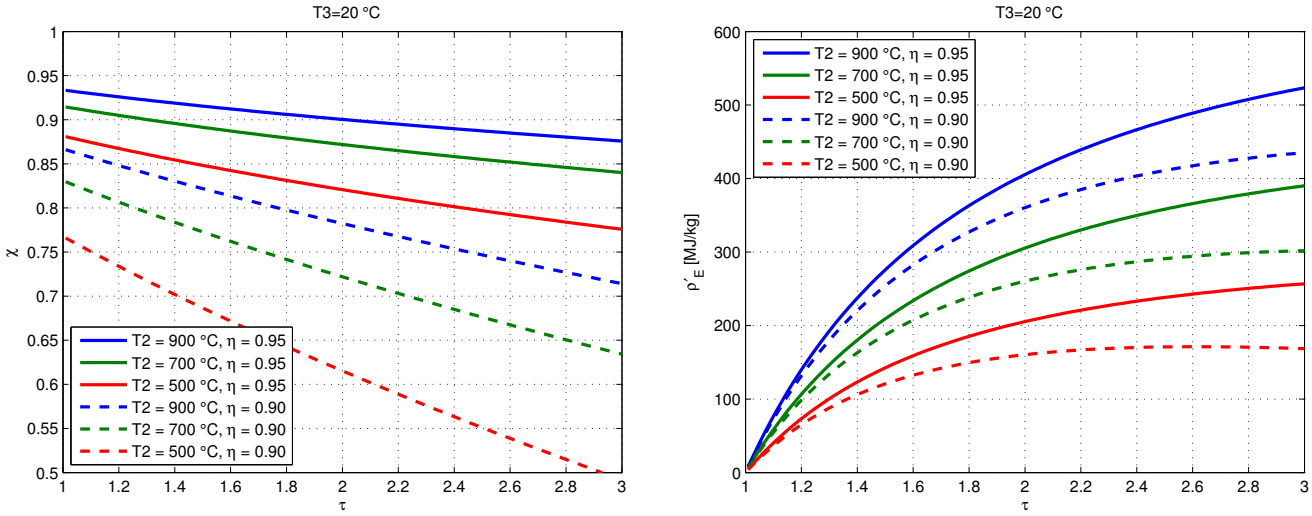

Figure 2.5: Impact of compressor/expander irreversibilities. Left: Maximum round-trip-efficiency χ as a function of the temperature ratio τ. Right: Discharge energy density ρ'_E as a function of τ. In both cases, three curves are presented for fixed values of T_2, at two different values of η. An arbitrary value of $\rho_s c_s = 2\,\mathrm{MJ/m^3K}$ has been used.

$$\rho'_E \equiv \chi \cdot \rho_E \tag{2.19}$$

ρ_E can be rewritten as:

$$\rho_E = \frac{1}{2}\rho_s c_s \left((T_2 - T_1) - (T_3 - T_4)\right) = \frac{1}{2}\rho_s c_s \left[T_2\left(1 - 1/\tau\right) - T_3\left(1 - \tau^{-\eta^2}\right)\right] \tag{2.20}$$

And therefore:

$$\rho'_E = \frac{1}{2}\rho_s c_s \left[T_2\left(1 - 1/\tau\right) - T_3\tau^{-\eta^2}\left(\tau^{1/\eta^2} - 1\right)\right] \tag{2.21}$$

Which is an increasing function with τ, but not as strong as Equation (2.2). The representations of Equations (2.18) and (2.21) are shown in Figure 2.5. The plots show the results for two different values of η and an assumed value of $\rho_s c_s = 2\,\mathrm{MJ/m^3K}$, although at this point we are not so interested on the absolute values but rather on the trends. The first thing to be concluded from Figure 2.5 is that the round-trip efficiency is very susceptible to changes in polytropic efficiency, although this effect can be greatly diminished by letting the maximum temperature T_2 increase. For a given value of T_2, a compromise has to be found between energy density and efficiency by selecting the appropriate temperature ratio τ. For systems that suffer from low values of both η and T_2, a low value of τ is recommended, since a big increase in the round-trip efficiency can be obtained with a comparatively low sacrifice on

energy density, while the opposite is true for systems with high values of η and T_2.

2.2.7 Impact of pressure losses

Pressure losses will occur in different magnitudes in all the components of the cycle: inside the compressor/expander, the pipes, the thermal tanks and the heat exchangers. Detailed analysis requires a knowledge of the size and the operating conditions of each component, but it is nonetheless interesting to evaluate the impact of these on the performance of the cycle. This can be done by defining an overall pressure loss factor, F, which, as noted in [10], will be approximately given by the sum of the fractional pressure losses in all component provided they are small. The overall pressure loss supposes a higher pressure ratio to be delivered by the compressor with respect to that of the expander:

$$\beta_e = (1 - F)\,\beta_c \tag{2.22}$$

Using (2.8) and $\tau \equiv \tau_c$ we obtain:

$$\tau_e = (1 - F)^{\phi_e}\,\tau_c^{\phi_e/\phi_c} = (1 - F)^{\frac{\eta(\gamma-1)}{\gamma}}\,\tau^{\eta^2}$$

Similarly for the case of the discharge cycle, using $\tau' \equiv \tau'_e$:

$$\tau'_c = (1 - F)^{-\phi_c}\,\tau_e'^{\phi_c/\phi_e} = (1 - F)^{\frac{-(\gamma-1)}{\eta\gamma}}\,\tau'^{1/\eta^2}$$

If the cycle is operated such that $\tau' = \tau$, then we know that $T_{2'} = T_2$, $T_{4'} = T_4$ and $T_{1'} = T_1$. Using the expressions above we can find the value of $T_{3'}$:

$$T_{3'} = T_3\,(1 - F)^{-(\phi_c+\phi_e)}\,\tau^{1/\eta^2-\eta^2}$$

We can now evaluate the impact on the round-trip efficiency. We can use Equation (2.10) expressed as a function of T_2:

$$\chi = \frac{w_{net,dis}}{w_{net,ch}} = \frac{T_2\,(1 - 1/\tau) - T_{3'}\,(1 - 1/\tau'_c)}{T_2\,(1 - 1/\tau) - T_3\,(1 - 1/\tau_e)} \tag{2.23}$$

and substitute the expressions shown above for τ_e, τ'_c and $T_{3'}$. For simplicity, the effect of F will be evaluated separately from compressor/expander irreversibilities by setting $\eta = 1$. This allows us to write:

$$\chi = \frac{T_2\,(1 - 1/\tau) - T_3\left[(1 - F)^{-2(\gamma-1)/\gamma} - \left((1 - F)^{(\gamma-1)/\gamma}\,\tau\right)^{-1}\right]}{T_2\,(1 - 1/\tau) - T_3\left[1 - \left((1 - F)^{(\gamma-1)/\gamma}\,\tau\right)^{-1}\right]} \tag{2.24}$$

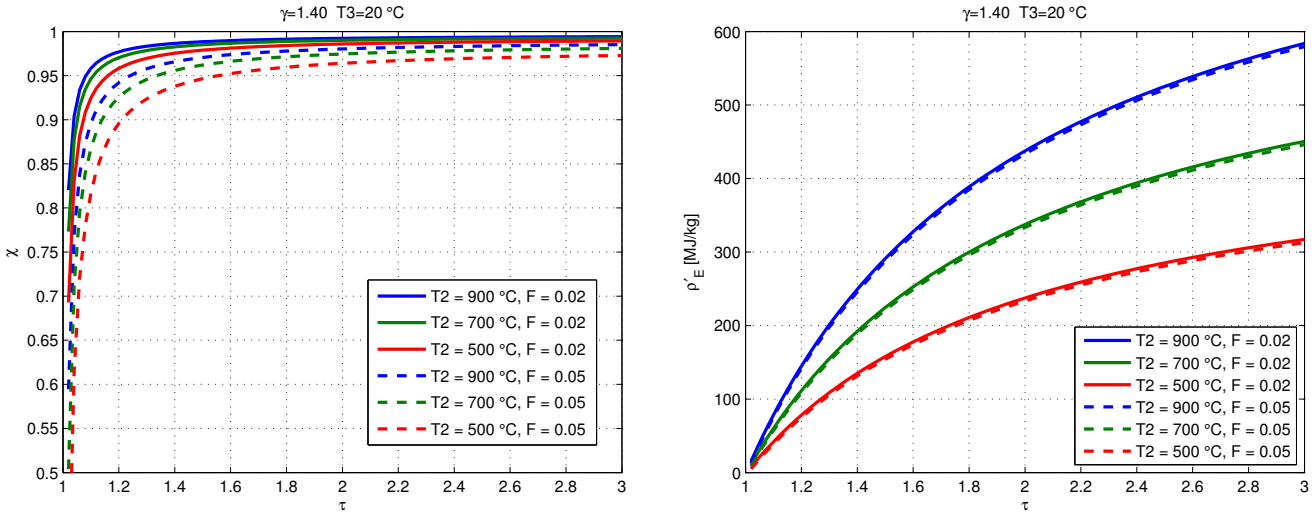

Figure 2.6: Impact of global pressure losses. Left: Maximum round-trip-efficiency χ as a function of the temperature ratio τ. Right: Discharge energy density ρ'_E as a function of τ. In both cases, three curves are presented for fixed values of T_2, at two different values of F. An assumed value $\rho_s c_s = 2\,\mathrm{MJ/m^3K}$ has been used.

And, in the case of the energy density:

$$\rho'_E = \frac{1}{2}\rho_s c_s \left[T_2 \left(1 - 1/\tau\right) - T_3 \left[\left(1-F\right)^{-2(\gamma-1)/\gamma} - \left(\left(1-F\right)^{(\gamma-1)/\gamma} \tau \right)^{-1} \right] \right] \tag{2.25}$$

These two expressions have been plotted in Figure 2.6. Comparing the left sides of Figures 2.5 and 2.6 we can notice that, while the impact of compressor/expander irreversibilities on χ can be minimized by lowering τ, the necessary strategy for minimizing the impact of pressure losses is the exact opposite. In practice this means that an optimal τ exists which minimizes the combined effect of both losses on χ. Finding this optimal τ, however, requires modelling of each component of the system to understand how the global fractional pressure loss, F, varies with operating conditions.

2.2.8 Impact of heat transfer over a finite temperature difference

Real power machines require work transfer and heat transfer processes to happen over relatively short amounts of time, easily departing from the ideal limits set by time-independent thermodynamics. In the case of heat transfer processes, this implies that a finite heat transfer rate is required over a limited contact surface, which, according to Fourier's law of heat conduction, can only be achieved through a finite temperature difference. A simple way to exemplify the impact of this temperature difference on TEES systems was presented by White in [13] and is briefly reproduced below.

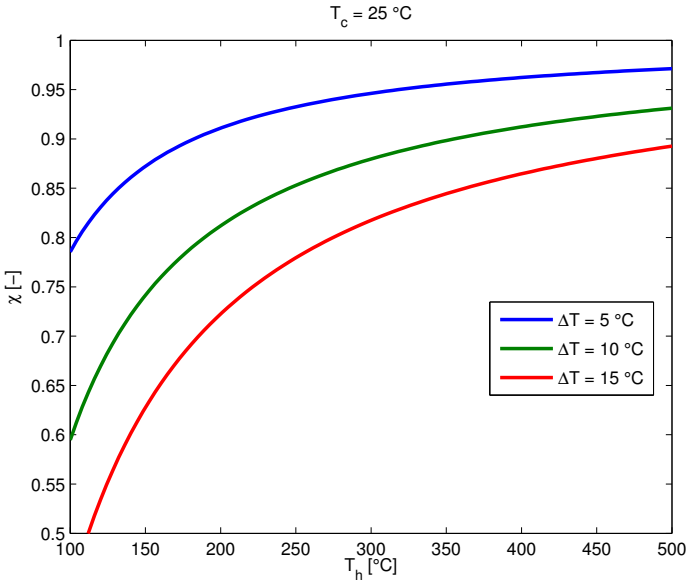

Figure 2.7: Maximum round-trip efficiency, χ as a function of T_h for three different values of ΔT. The temperature of the cold reservoir has been set to ambient in this case, $T_c = 25\,°C$.

Consider the generic TEES system from Figure 1.1, constituted by a heat pump and a heat engine that operate between two thermal reservoirs, one at T_h and the other at T_c. As explained in section 1.2.1, the ideal round-trip efficiency of such a system is one, provided both the heat pump and the heat engine are ideal reversible devices. Consider now the temperature difference, ΔT, that occurs between the working fluid and the storage media during heat transfer. The heat pump will *effectively* operate between $T_{c,eff} = T_c - \Delta T$ at the cold side and $T_{h,eff} = T_h + \Delta T$ at the hot side, while the heat engine will operate between $T_{c,eff} + \Delta T$ and $T_{h,eff} - \Delta T$. The maximum round trip efficiency becomes (considering that all other processes are reversible):

$$\begin{aligned}\chi = COP \cdot \eta &= \left(\frac{T_{h,eff}}{T_{h,eff} - T_{c,eff}}\right)_{pump} \cdot \left(\frac{T_{h,eff} - T_{c,eff}}{T_{h,eff}}\right)_{engine} \\ &= \left(\frac{T_h + \Delta T}{T_h + 2\Delta T - T_c}\right) \cdot \left(\frac{T_h - 2\Delta T - T_c}{T_h - \Delta T}\right)\end{aligned}$$

A plot of this expression is shown in Figure 2.7 for a fixed value of T_c. It is seen how χ decreases rapidly for increasing values of ΔT, and how the way to minimize this effect is by increasing the value of T_h. Nevertheless, the maximum temperature, T_h, will normally be limited by material constraints of the components exposed to it. ΔT, on the other hand, will depend on the mechanism used to drive heat transfer between the working fluid and the storage media, which may be direct contact between gas and solid in packed-bed reservoirs,

or through a heat exchanger in the case of liquid storage media. A heat exchanger model that is being developed to study this and other issues is presented in section 3.2.

2.3 The Joule-Brayton cycle with liquid storage media

During the last few years, the research group to which the author of this report belongs has focused research efforts on the thermodynamic cycle for energy storage described in [12, 11], which is based on the JB cycle and uses a solid material (typically a packed bed of particles or a matrix of ceramic) as storage medium. The thermal energy is stored in the form of sensible heat, typically taking advantage of materials that have high densities, high specific heat capacities and that can operate along a wide range of temperature conditions. This leads not only to a storage medium with high volumetric energy density but also brings flexibility when designing the operating conditions of the thermodynamic cycle (which, for instance, can maximize the round-trip efficiency or minimize the capital cost). Other advantages of the proposed solid storage media include the fact that they may be made of cheap, abundant materials that are harmless to the environment. On the other hand, the gas-solid heat exchange within the reservoir process generates a thermal front that deteriorates over time. This decreases the amount of energy that can be recovered (limiting the energy density of the tank) and has a significant negative impact on the round-trip efficiency, specially when long storage periods are necessary. A possible approach to tackle this problem, known as reservoir segmentation, is being studied, and more details are presented in section 3.5. Another disadvantage is that the hot reservoir has to be pressurized at the same level than the working fluid at that part of the cycle, which notably increases the capital cost of the tank.

In the case of systems that use liquid storage media, heat is normally transmitted by means of a heat exchanger between the working fluid and the storage liquid, while the latter is being pumped from its initial reservoir (at the discharged temperature) to its final reservoir (at the charged temperature). Such a scheme ensures that thermal gradients are contained within the heat exchanger and that the thermal tanks stay at a single temperature each. Therefore, losses inside the reservoirs during the storage period become only a function of the degree of insulation and independent of the operation history, what makes operation strategies more flexible. For these reasons, they are specially attractive for those applications that may require energy storage over longer periods of time (from days to weeks, for instance, as would be the case when trying to compensate for wind energy fluctuations).

Liquid storage media is the strategy most commonly used in Concentrated Solar Power (CSP) plants that have energy storage capability, where the state of the art technology consists of two-tank molten salt systems [21]. The left hand side of Figure 2.8 shows a simplified layout of a CSP plant with an integrated liquid TES using the two-tank system. Since CSP

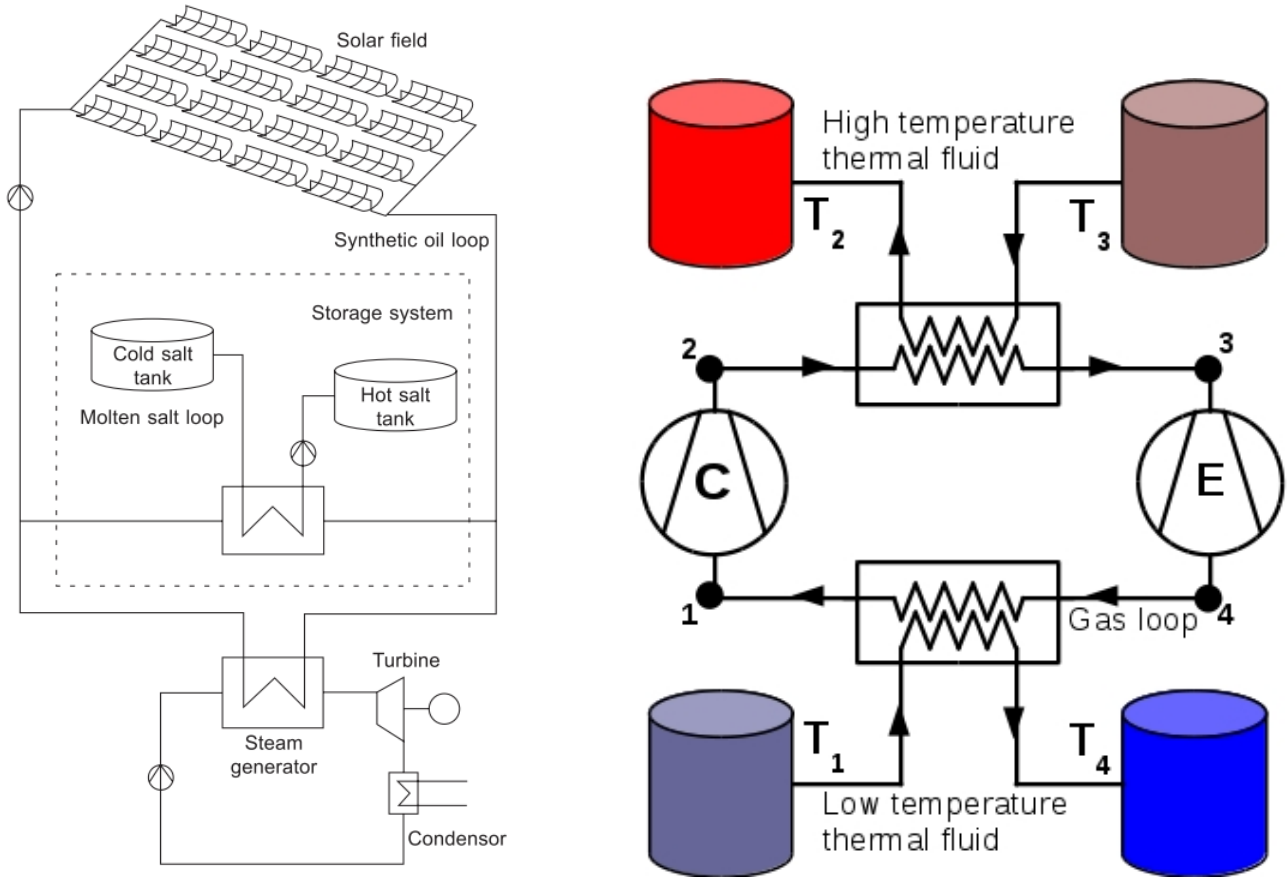

Figure 2.8: Left: Layout of a CSP plant based on the Rankine cycle and incorporating a two-tank molten salt thermal storage system. From source: [21]. Right: Layout of a TEES system using the JB cycle and liquid storage media.

plants normally operate using the Rankine cycle, heat injection in the steam generator occurs at the nominal temperature needed to drive the turbine, while heat rejection occurs as close as possible to ambient temperature during the condensation stage. This means that a single TES system is necessary for energy storage, which should operate at the same temperature than the nominal temperature of the turbine.

On the other hand, the closed JB cycle needs both a high temperature storage and a cold temperature storage, since it does not consist of any isothermal stage that can exchange heat with the environment at a temperature close to ambient temperature. Therefore, in the case of using liquid storage media, two pairs of liquid reservoirs would be needed, as shown in the right hand side of Figure 2.8.

Suitable liquid media and configuration strategies will be discussed in the following sections.

2.3.1 Suitable materials and temperature constraints

The feasibility of a thermodynamic cycle that uses liquid storage media depends on the successful identification of substances that maintain adequate properties along the desired temperature conditions. The selected materials should not only be able to remain liquid (and stable) within wide temperature ranges (and without excessive pressurization), but also have a high volumetric specific heat capacity, be relatively cheap and abundant, and ideally harmless to the environment.

A list of potentially suitable liquids has been made and their main thermophysical and transport properties have been collected from the literature. Results are presented in Table 2.1. Data is presented for the melting point T_{min}, the boiling point (or maximum stability point, or smoke point) T_{max}, density ρ, specific heat capacity c_p, viscosity μ and thermal conductivity κ. Sometimes data of a certain property appears as an average value, as an specific value at a certain temperature, or as the two extreme values close to T_{min} and T_{max}. Linear average values of ρ and c_p are used to estimate the specific heat capacity in volumetric terms, $\rho \cdot c_p$. Also, an estimate of the maximum volumetric energy density is given by computing $\rho \cdot c_p \cdot (T_{max} - T_{min})$. Note that, in this case, a maximum value of 25 °C is sometimes used instead of T_{max} for liquids that would be used in the cold thermal tanks, and a minimum value of also 25 °C instead of T_{min} for liquids that would be used in the hot thermal tank. In this latter case, an hypothetical maximum limit of 1300 °C is used instead of T_{max} for liquids that have very high boiling points.

The following is a list of the references used to obtain data from each substance.

		Name and Composition	T_{min} [ºC]	T_{max} [ºC]	ρ [kg/m³]	C_p [J/(g·K)]	μ [mPa·s]	κ [W/m·K]	$\rho*C_p$ [MJ/(m³·K)]	$\rho*C_p*(T_{max} - T_{min})$ [MJ/m3] (kWh/m3)
COLD TANKS	Hydrocarbons	Butane C4H10	-134	-1 (1bar) 50 (5bar) 78 (10bar)	730 – 602	1.98 – 2.31	1.89 – 0.204	0.175 – 0.116	1.43	190 (53) (till -1ºC) 227 (63) (till 25ºC)
		Pentane C5H12	-129	35 (1bar) 92 (5bar) 125 (10bar)	756 – 611	1.86 – 2.31	3.77 – 0.229	0.178 – 0.145	1.43	220 (61) (till 25ºC)
	Alco-hol	Ethanol C2H6O	-114	78 (1bar) 126 (5bar) 152 (10bar)	900 – 734	1.81 – 2.92	>60 – 0.43	0.21 - 0.15	1.93	268 (75) (till 25ºC)
HOT TANKS	Water	Water H2O	0	100 (1bar) 152 (5bar) 180 (10bar)	1000 – 960	4.20 – 4.22	1.7 – 0.28	0.56 – 0.68	4.13	310 (86) (from 25 till 100ºC) 516 (143) (from 25 till 150ºC)
	Oils	Sunflower oil	-16	209 (smoke point)	920	1.8 – 2.2	-	-	1.84	339 (94) (from 25ºC)
		Mineral oil	-	340	770	2.6	-	0.12	2.00	630 (175) (from 25ºC)
		Therminol VP-1 diphenyl-biphenyl ox-ide	12	257 (1bar) 400 (max) (10bar)	1060	1.78 (100ºC)	2.63 (40ºC)	0.128 (100ºC)	1.89	709 (197) (from 25 till 400ºC)
	Molten salts	Saltstream XL $NaNO_3$ + KNO_3 + $Ca(NO_3)_2$	120	500	1870 (450ºC)	1.45 (300ºC)	1.63 (450ºC)	0.52 (450ºC)	2.71	1030 (286)
		HITEC HTS $NaNO_2$ + $NaNO_3$ + KNO_3	142	450	1940 (200ºC) 1750 (450ºC)	1.55 (300ºC)	16 (150ºC) 2.0 (375ºC)	0.44 (149ºC) 0.30 (450ºC)	2.86	881 (245)
		Solar salt $NaNO_3$ + KNO_3	230	550	1950 – 1750	1.55 – 1.55	5.8 – 1.9	0.46 – 0.57	2.87	918 (255)
		Saltstream 565 Primarily Nitrates	246	565	1920 (300ºC)	1.51 (300ºC)	-	-	2.90	925 (257)
		Saltstream 700 Primarily Chlorides	257	700	2310 (300ºC)	0.79 (300ºC)	16.9 (300ºC) 1.0 (700ºC)	-	1.82	806 (224)
	Glass	Haloglass RX Glass oxides	450	1200	2400	1.36 (450ºC)	10000 (450ºC) 1000 (580ºC) 11 (1200ºC)	0.8	3.26	2445 (679) (from 450ºC) 1955 (543) (from 600ºC)
	Metals	Sodium Na	98	883	808	1.25	0.21	46	1.01	793 (220)
		Lead-Bismuth (eutectic) PbBi	125	1533	9660	0.15	1.1	12.8	1.45	1700 (473) (till 1300ºC)
		Tin Sn	232	2602	7000 – 5500	0.248 (232ºC)	1.966 (232ºC)	30.3 (232ºC)	1.55	1655 (460) (till 1300ºC)
		Lead Pb	327	1749	10200 – 9000	0.148 – 0.135	2.555 (338ºC)	15.5 (660ºC)	1.36	1320 (368) (till 1300ºC)
		Zinc Zn	420	912	6500 – 6000	0.48 (420ºC)	3.461 (420ºC)	49.5 (420ºC)	3.00	1475 (410)
		Aluminium Al	658	2515	2400 – 2200	1.18 (660ºC)	1.39 (660ºC)	90.7 (660ºC)	2.71	1740 (483) (till 1300ºC)

Table 2.1: Main properties of liquids attractive for heat transfer and/or thermal energy storage. Compilation from several sources (see text in section 2.3.1 for references).

Material	Ref.:	Material	Ref.:	Material	Ref.:
Butane	[22]	Sunflower oil	[23, 24, 25]	HITEC HTS	[26]
Pentane	[27, 28]	Mineral oil	[29, 21]	Solar salt	[30, 31]
Ethanol	[32, 28]	Therminol VP-1	[33]	Haloglass RX	[34]
Water	[22]	Saltstream XL, 565 & 700	[34]	Molten metals	[35, 27, 29]

Five families of liquids that could be suitable for the hot reservoirs appear in Table 2.1. Water is the first one, and certainly the most attractive liquid for heat transfer and thermal energy storage applications at temperatures up to 100 °C, since it is extremely abundant, harmless and has the highest volumetric specific heat capacity ($\rho \cdot c_p$) among all the other liquids presented. For temperatures above 100 °C, however, pressurization becomes necessary, dramatically increasing the cost of the thermal tanks.

The second family consists on oils. The first one, Sunflower oil, is a cheap an abundant liquid that comes from a renewable source, although its maximum operating temperature is relatively low compared to that of other oils from mineral or synthetic origin. The smoke point of Sunflower oil is just above 200 °C. The first commercial CSP plant, SEGS-1, used mineral oil both as a heat transfer fluid (between the absorbers of the parabolic troughs and the steam generator) and as an energy storage medium [21], allowing operation close to 340 °C. Nevertheless, subsequent plants mainly use a synthetic oil named Therminol VP-1, enabling temperatures of almost 400 °C. While Therminol VP-1 is commonly used as the heat transfer fluid, it is too expensive for bulk thermal energy storage; instead of oil, molten nitrates are currently the most common storage fluid in commercial CSP plants [29].

Molten salts possess several characteristics that make them favourite for bulk thermal energy storage applications for power generation. Compared to other liquids, their production costs are normally low [29]. They have low vapour pressures and high heat capacities per unit volume. The most common energy storage fluid used in CSP plants nowadays is a molten salt known as Solar salt, a binary mixture with 60 wt% sodium nitrate ($NaNO_3$) and 40 wt% potassium nitrate (KNO_3) [30]. The Solar salt melts at 230 °C and has a maximum stability point around 550 °C, at which it starts to decompose. Adding other compounds to the mixture allows to reduce the melting point of the mixture, as in the case of adding calcium nitrate ($Ca\,(NO_3)_2$). Halotechnics Inc. claims that their Saltstream XL ternary mixture is an "unbeatable combination of price an performance", due to its lower melting point at 120 °C and the fact that it is made of earth abundant components [34]. Another more traditional combination, the HITEC HTS, a ternary mixture of sodium nitrate, potassium nitrate and sodium nitrite ($NaNO_2$), with a melting point of 142 °C, is more commonly used as a heat transfer fluid rather than as a fluid for bulk energy storage, due to the higher price of the

sodium nitrite component [21].

Halotechnics Inc. is also developing thermal energy storage fluids to operate in higher temperature ranges. Their Haloglass RX material, a fluid constituted of glass oxides, melts at 450 °C and its thermal stability reaches 1200 °C. Nevertheless, its extremely high viscosity at temperatures close to its melting point could possibly restrict its operative temperature range to temperatures of 600 °C or above. An analysis of the pumping power needed to transport the fluid from one tank to the other and through the heat exchanger is necessary to better evaluate the practicality of using this fluid at different temperatures.

Molten metals are the last family of fluids that are included in table 2.1 as candidates for heat transfer and thermal energy storage applications. They are characterized by very high thermal conductivities, low viscosities, and extremely wide temperature ranges over which they stay in the liquid form. Nevertheless, they tend to be expensive and have high melting points. Sodium comes first in the group, being a very abundant element with a melting point as low as 98 °C. The main problem with sodium is its high reactivity and the exothermic reaction that it presents with water, with release of hydrogen [29]. Therefore, the use of liquid sodium for bulk thermal energy storage would increase material costs and safety requirements of the plant. An eutectic mixture of lead and bismuth obtains a melting point of only 125 °C. Nevertheless, Bismuth is a scarce material, and the capital costs of using it as a bulk material could be prohibitive. Lead alone has its melting point at 327 °C. Despite its toxicity, it is widely used in electrochemical batteries for distributed energy storage. Interestingly enough, lead can achieve higher volumetric energy densities by storing sensible heat than the energy densities it normally presents in electrochemical lead-acid batteries (around 100 kWh/m^3). The last metal to be included is aluminium. Despite having the highest melting point in the list (658 °C), it is included in virtue of being the most common metal in the earth's crust and having a very high thermal conductivity, high volumetric specific heat capacity and low viscosity.

On the other hand, only three liquids appear in the table that could be used to store energy energy on the cold side of the cycle. In fact, existing refrigerants amount to hundreds of different substances, and a systematic search for the most adequate material is yet to be done. Nevertheless, the three substances that appear in the table have been selected because they are relatively common in several industrial or domestic applications and the temperature ranges at which they stay liquid are adequate. In particular, ethanol seems a very attractive candidate, both for its comparatively high volumetric specific heat capacity and the fact that it may be produced from biological sources.

2.3.2 Operating strategies

Consider the ideal T-s diagram of the JB cycle for energy storage presented in the right hand side of Figure 2.1, with $T_1 = T_3 = 25\,°C$, $T_2 = 500\,°C$ and $T_4 \approx -160\,°C$. Consider that the selected method to store the thermal energy was the liquid tanks system, as shown in the right hand side of Figure 2.8. Note that none of the liquids presented in Table 2.1 would be able to cover by itself the temperature range required between T_3 (ambient temperature) and the top temperature T_2. Nevertheless, some strategies can be developed to solve this problem, which are presented below.

2.3.2.1 Coupling of liquid thermal reservoirs in series

The easiest way to expand the temperature range over which the JB cycle could operate when having liquid reservoirs is to use more than one liquid in series, as exemplified in Figure 2.9. This would allow, for example, to use pressurized water between $T_3 = 25\,°C$ and $T_{2b} = 140\,°C$, and a low melting point molten salt compound like Saltstream XL between $T_{2b} = 140\,°C$ and $T_2 = 500\,°C$, therefore covering all the necessary range between T_3 and T_2. Another possibility would be to use a vegetable oil between ambient temperature and about $200\,°C$, and ternary mixture based on the Solar salt (for example, including some amount of $Ca\,(NO_3)_2$ or $NaNO_2$) which lowered its melting point just enough to be able to cover the range between $200\,°C$ and $500\,°C$.

The expressions of the maximum round-trip efficiency χ as a function of compression/expansion irreversibilities and overall pressure loss, as derived in section 2.2, do not change in the case being currently considered. The expression of the charge energy density ρ_E does change, however, as now we have three different storage materials, two on the hot side and one on the cold side of the cycle. Starting again from Equation (2.1), and following the same procedure and assumptions stated in section (2.2.3):

$$\rho_E = \frac{E_{net}}{V_{HS} + V_{CS}} = \frac{\Delta E_{HS1} + \Delta E_{HS2} + \Delta E_{CS}}{m_{HS1}/\rho_{HS1} + m_{HS2}/\rho_{HS2} + m_{CS}/\rho_{CS}} \tag{2.26}$$

Where the indexes $HS1$ and $HS2$ refer to the liquids in the hot stores 1 and 2, and CS refers to the liquid in the cold store. The mass of liquid m_l which is necessary to capture the change in sensible energy from a certain mass of gas m_g while experiencing the equivalent (but opposite) temperature variation is given by:

$$m_l = \frac{m_g c_{p,g}}{c_{p,l}} \tag{2.27}$$

Knowing that the same mass of gas is circulated through the three heat exchangers, and assuming that the gas may be treated as a perfect gas (i.e. with constant $c_{p,g}$):

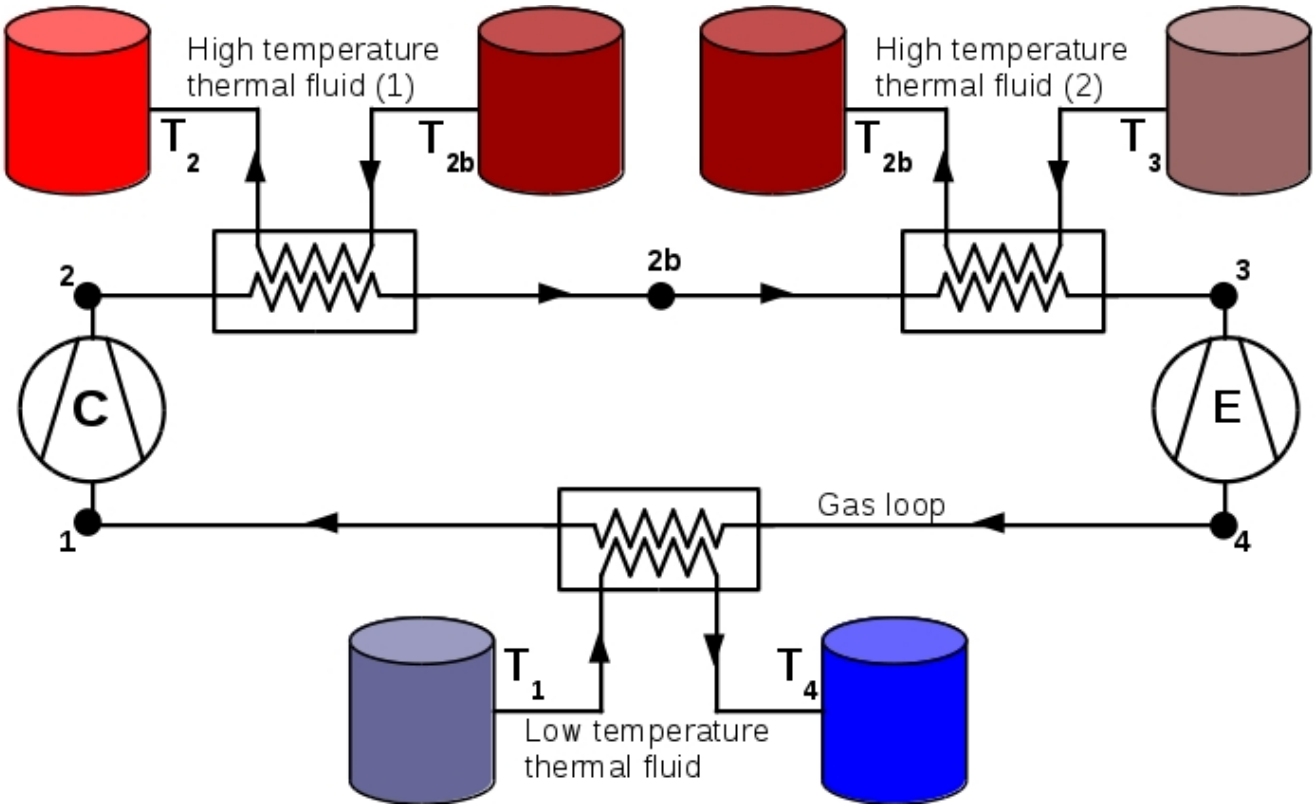

Figure 2.9: Layout showing the coupling in series of two different liquid media for storing thermal energy in the high temperature part of the cycle.

$$\rho_E = \frac{m_g c_{p,g} \left(\Delta T_{HS1} + \Delta T_{HS2} + \Delta T_{CS}\right)}{m_g c_{p,g} \left(1/\left(c_{p,HS1}\,\rho_{HS1}\right) + 1/\left(c_{p,HS2}\,\rho_{HS2}\right) + 1/\left(c_{p,CS}\,\rho_{CS}\right)\right)} \tag{2.28}$$

Including the cycle temperatures, and noting that T_{2b} cancels:

$$\rho_E = \frac{(T_2 - T_3) - (T_1 - T_4)}{1/\left(c_{p,HS1}\,\rho_{HS1}\right) + 1/\left(c_{p,HS2}\,\rho_{HS2}\right) + 1/\left(c_{p,CS}\,\rho_{CS}\right)} \tag{2.29}$$

Finally, it is instructive to show that, if the three liquids happened to have the same volumetric heat capacity, $c_{p,l}\rho_l$, and it was constant, then the expression of the energy density would simplify to:

$$\rho_E = \frac{1}{3} c_{p,l}\rho_l \left[(T_2 - T_3) - (T_1 - T_4)\right] \tag{2.30}$$

Which is the equivalent of Equation (2.2) but with a factor of $1/3$ rather than $1/2$, as should have been expected.

2.3.2.2 Stage repetition

The strategy that has just been presented (coupling liquid thermal reservoirs in series) allows us to design a system that can cover the whole temperature range between T_3 at ambient temperature and $T_2 = 500\,°\text{C}$. Note, however, that if we have $T_1 = T_3 = 25\,°\text{C}$, then $\tau = T_2/T_1 \approx 2.6$. Using Equation (2.11) we can write $T_4 = T_3/\tau\eta^2$, and this means that T_4 would range between $-135\,°\text{C}$ and $-158\,°\text{C}$ in the case of η ranging between 0.9 and 1.0. None of the three refrigerants from Table 2.1 have a melting point which is low enough to cover this temperature range. Without making any assumptions on the suitability (in terms of price, abundance, safety, etc.) of other refrigerants that could possibly cover the whole range, it is interesting to devise a strategy which can solve this problem.

The method consists on breaking the expansion stage into two equal sub-stages, as shown in the upper part of Figure 2.10. This allows the compressor to operate at the same temperature ratio as before while reducing the temperature ratio in each of the expansion sub-stages, therefore increasing the value of T_4. A T-s diagram of the considered cycle is shown in the left lower corner of the same Figure, where it is shown that T_4 has a value above $-100\,°\text{C}$ when the expansion is divided into two sub-stages.

To evaluate the impact of implementing this method on the maximum round-trip efficiency of the system, χ, it is necessary to follow again a derivation similar to that presented in section 2.2.6. This is a straightforward but long procedure and only the final expression will be presented. The differences from the former derivation are the following:

- The work performed by the expander is multiplied by a number of expansions n.

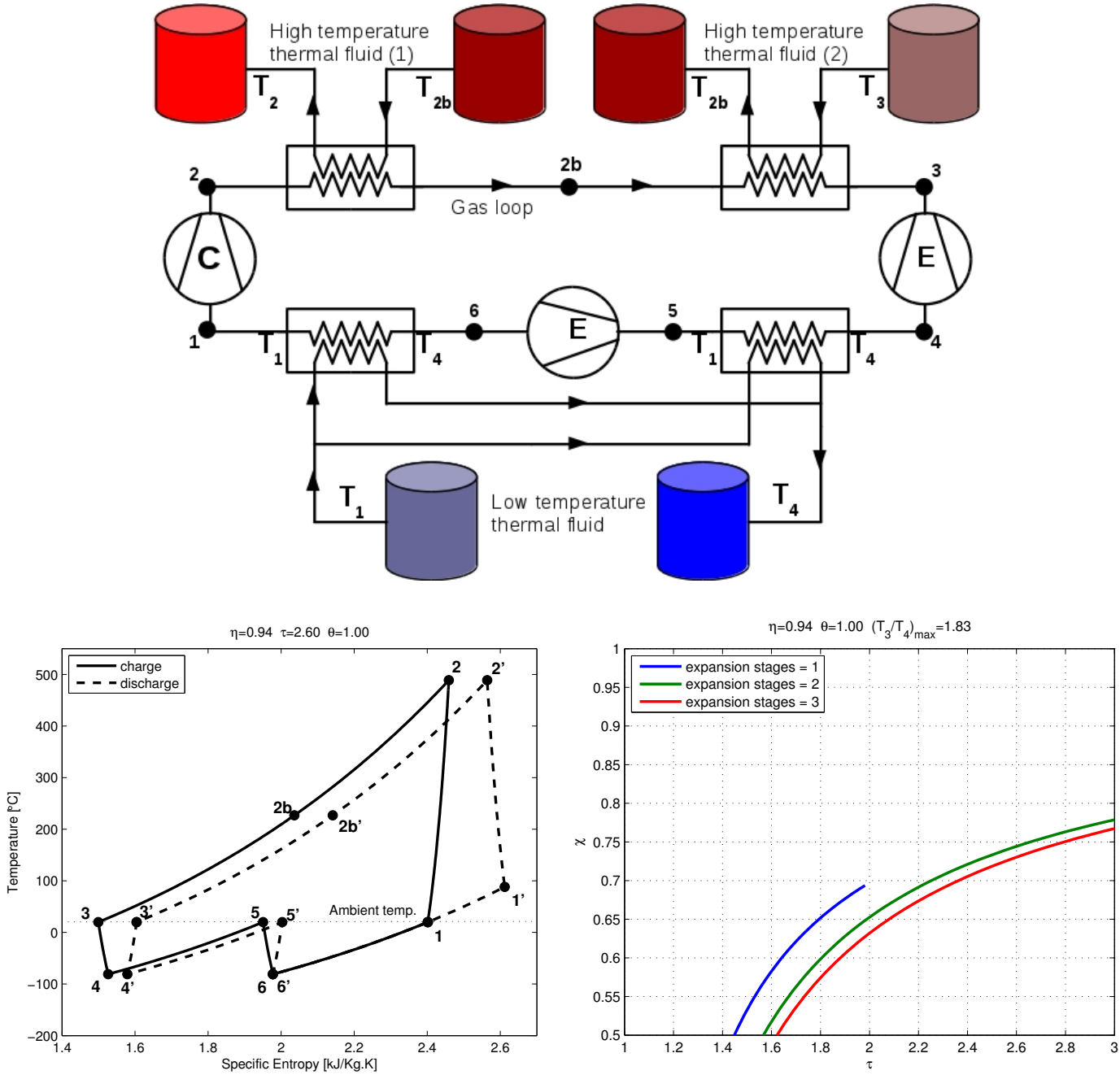

Figure 2.10: Above: Layout showing the coupling in series of two different liquid media for storing thermal energy in the high temperature part of the cycle, and division of the expansion stage in two sub-stages for storing thermal energy in the low temperature part of the cycle. Below, left: T-s diagram of the considered cycle. Below, right: plot of the efficiency as a function of τ comparing the cycle with either one, two or three equal expansion stages.

- The temperature ratio $\theta = {}^{T_3}/_{T_1}$ is set to 1 (i.e. both T_1 and T_3 are assumed to be at ambient temperature).
- Heat rejection to the environment is assumed to happen between $T_{1'}$ and T_1, and therefore the discharge temperature ratio is set to $\tau' = \tau'_{min} = \tau^{\eta^4}$.
- A limit on the maximum temperature of the cycle, T_2, is not included and therefore increasing τ implies increasing T_2.
- The equation can be expressed as a function of τ or as a function of $\tau_e = {}^{T_3}/_{T_4}$. The relationship between τ_e and τ for a generic number of expansions n is $\tau = \tau_e^{n/\eta^2}$.

The result is:

$$\chi = 1 - \frac{\tau_e^{n\left(1/\eta^2 - \eta^2\right)} - 1}{\tau_e^{n/\eta^2} - 1 - n\left(1 - {}^1/_{\tau_e}\right)} = 1 - \frac{\tau^{\left(1-\eta^4\right)} - 1}{\tau - 1 - n\left(1 - \tau^{-\eta^2/n}\right)}$$

The plot of this function for $n = 1, 2, 3$ and an arbitrary value of the polytropic efficiency $\eta = 0.94$ is presented in the right lower corner of Figure 2.10. In the same plot it has been assumed that the minimum possible value of T_4 is $-110\,°\text{C}$ (limited by the freezing point of the refrigerant) and therefore the maximum value of the expansion temperature ratio is $\tau_e = {}^{T_3}/_{T_4} = 1.83$. Note that, for a given value of τ, dividing the expansion stage in two or three sub-stages has a *negative* impact on the efficiency χ. Nevertheless, dividing the expansion stage allows having higher temperature ratios in the compression stage (reaching higher top temperatures), which has a *positive* impact on the efficiency. In the example considered, setting a limit on τ_e of 1.83 while having only one expansion stage means that the maximum value of τ is around 2; i.e. $T_2 \approx 320\,°\text{C}$ and $\chi \approx 0.7$. Having two expansion stages allows to have a much higher maximum value of τ, around $\tau \approx 3.9$, which would bring T_2 up to almost $900\,°\text{C}$. For comparison, setting the maximum system temperature $T_2 = 500\,°\text{C}$ as in previous examples would mean $\tau \approx 2.6$ and $\chi \approx 0.75$.

2.3.2.3 The gas-gas heat exchanger bypass

The two strategies presented so far allow us to configure a system that can operate from $T_1 = 25\,°\text{C}$ to $T_2 = 500\,°\text{C}$ despite the temperature constrains that the liquid media present. Nevertheless, these strategies have increased the complexity of the cycle and multiplied by two the number of thermal tanks. Now we present another approach which keeps the system simple, the number of components low, and the efficiency high. It consists on lowering the value of θ (i.e. setting $T_1 > T_3$) and implementing a gas-gas heat exchanger (recuperator) between T_1 and T_3 as shown in Figure 2.11.

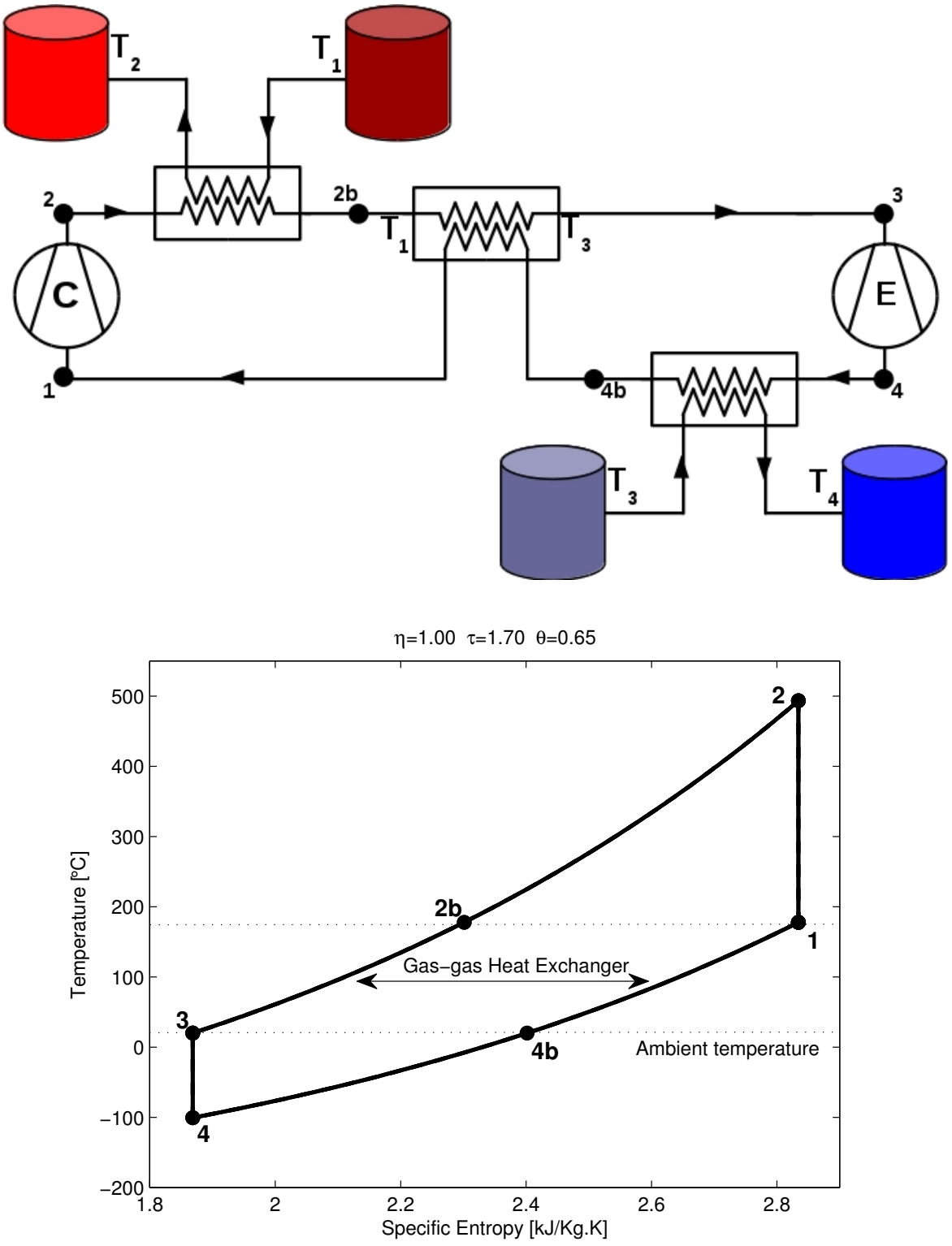

Figure 2.11: Above: Layout showing the implementation of a gas-gas heat exchanger between points 2b and 4b (temperatures T_1 and T_3). Below: Ideal T-s diagram of the considered cycle.

The recuperator acts as a "bypass", recuperating thermal energy from the high pressure gas at T_1 (point 2b) and transmitting it to the low pressure gas at T_3 (point 4b). This makes the selection of storage materials more flexible, since they do not need to stay in the liquid form between T_3 and T_2, but only between T_1 and T_2. The only operational difference is that the hot thermal tank stays above ambient temperature when discharged (T_1).

Note that the energy density of the system, ρ_E, depends on the value of $(T_2 - T_1) - (T_3 - T_4)$ (see, for example, Equation (2.2)), and is therefore independent on whether the thermal energy released by the gas while going from T_1 to T_3 in the high pressure side, and absorbed from T_3 to T_1 in the low pressure side, is stored separately and recovered during discharge or directly transmitted from one side to the other through a recuperator. Additionally, increasing the value of T_1 has a positive effect on the round-trip efficiency, as it was noted earlier. Nevertheless, the heat exchangers have a penalty in the form of pressure loss and effectiveness, which is currently under investigation.

By using a HEX, both T_2 and T_1 can be adapted according to the maximum stability point and melting point of the hot thermal fluid. For example, Solar salt could be used between $T_1 = 230\,°\text{C}$ and $T_2 = 550\,°\text{C}$ (in practice, T_1 would be slightly higher and T_2 slightly lower than these values, as some margin has to be left to ensure that neither melting nor decomposition occurs). This implies $\tau \approx 1.6$. Since $T_4 = {}^{T_3}/_{\tau_e} = {}^{T_3}/_{\tau\eta^2}$, we have $T_4 \approx -69\,°\text{C}$ for $\eta = 0.9$ and $T_4 \approx -87\,°\text{C}$ for $\eta = 1.0$). In this case, any of the three refrigerants presented in 2.1 would be compatible with the selected temperature range and stage repetition on the expander side would not be necessary.

Such a scheme would also allow to work with substances that are liquid only in higher temperature ranges. For example, zinc, which is an abundant metal and has a similar volumetric specific heat capacity than nitrate-based molten salts, could be used in the range between 420 °C and 900 °C, leading to very high energy densities and improved round-trip efficiencies (because of the high T_2 and moderate τ, see Figure 2.5). Even higher values of T_2 could be achieved by using, for instance, glass oxides or molten aluminium as storage media. Nevertheless, working at such high temperatures places material constraints and impacts the cost of the other components of the cycle. Fortunately, high temperature heat exchangers that are made with ceramic materials exist on the market. For instance, Heat Transfer International produces ceramic air-to-air heat exchangers that can operate up to 1300 °C and 13 bar [36]. Industrial gas turbines can operate at even higher temperatures, thanks to the use of advanced alloys, thermal barrier coatings, and internal cooling of the blades [37].

The choice between a medium temperature or high temperature scheme will depend on the efficiencies of available compressor/expander devices. Reciprocating compressors and expanders are receiving attention by various research groups (including our group at CUED

div-A, together with collaborators from Imperial College and Isentropic Ltd) because of their potentially higher polytropic efficiencies than turbomachines. Although top values are yet to be confirmed, high polytropic efficiencies (around 0.95 or above) would enable systems operating at medium temperature ranges to still show decent round-trip efficiencies. This option would be in principle preferred as to avoid the use of more expensive materials for the several system components. Nevertheless, if reciprocating devices fail to achieve such high polytropic efficiencies, then the higher values of round-trip efficiency and energy density provided by high temperature schemes will most probably pay back.

2.4 Variations of the Rankine cycle for electricity storage

Previous sections have focused attention on variations of a TEES system based on the JB cycle. Particularly, section 2.2.6 has shown that irreversible processes occurring in the compressor/expander, expressed by means of a polytropic efficiency η, have a big impact on the round-trip efficiency of the cycle. We have also seen that this effect is minimized when the work ratio between the turbine and the compressor is maximized. Unfortunately, reaching high values of work ratio in the JB cycle is not easy, as it involves either increasing the top temperature of the cycle T_2 (which is limited by material constraints) or by reducing the temperature ratio τ (but doing this decreases the energy density of the system as well as the power density, and increases the impact of pressure losses).

The work ratio of a Rankine cycle operating between a top temperature T_2 and a minimum temperature T_4 is inherently bigger than the work ratio of a JB cycle operating between the same limits, as the compression and expansion processes of the Rankine cycle happen in two different phases of the working fluid (see the generic T-s diagram is shown in Figure 2.12 for reference). This effect can be better understood by reminding that the work involved on a reversible compression or expansion process is $\delta w_{rev} = {}^{-dp}/_{\rho}$ (see section 2.2.5 for more details), and noticing that the density of the liquid phase is much larger than the density of the gaseous phase. Therefore, the work ratio tends to be high and the impact of compression/expansion irreversibility is lower than in the JB cycle, which makes it attractive.

Sections 2.4.1 and 2.4.2 will review TEES schemes based on the Rankine cycle that have been proposed in the literature. In section 2.4.3, the potential of using the steam cycle both as a heat pump and a heat engine is discussed and some key technologies that could enable such system are identified. Some final remarks are done in 2.4.4.

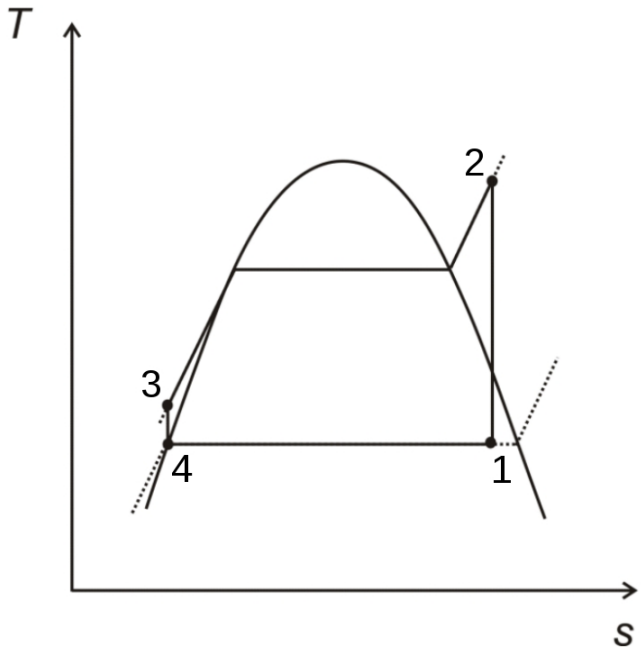

Figure 2.12: Generic T-s diagram of a Rankine Cycle. The number convention has been adapted to be consistent with the diagram of the JB cycle from Figure 2.1. Diagram from: [38].

2.4.1 Proposed systems using water/steam (only for discharge)

The most traditional use of the Rankine cycle is power generation, typically employing water/steam as the working fluid. It is a very widespread and mature technology and can receive the heat input from any external heat source which can reach an adequate temperature level, from coal fire to biomass, nuclear power or CSP. When run in reverse mode, the Rankine cycle may be used either as a heat pump or as a refrigerator, in which case the water is substituted by another working fluid which has a lower boiling point.

Here we are concerned with thermodynamic cycles for TEES systems, and it is therefore interesting to investigate the possible ways in which the Rankine cycle (or a variation of it) may be applied for such purposes. One of the simplest possible configurations uses an electric resistor during charge and the water/steam cycle during discharge. At least two versions of such a scheme have been suggested so far, both using sensible heat storage, one considering a single tank of bulk solid storage material and another one considering a two-tank molten-salt system [6, 39]. See a layout in Figure 2.13. The scheme is simple, the technologies are mature and the storage media may be a bulk material, therefore suggesting that this could be a cost-effective system. On the other hand, the COP of an electrical resistor is always 1, therefore limiting the round-trip efficiency of such a system to the efficiency of the (discharge) Rankine cycle. The *thermodynamic* efficiency (i.e., before mechanical and electrical losses are applied) of an industrial water/steam power station is normally below 50 % [38].

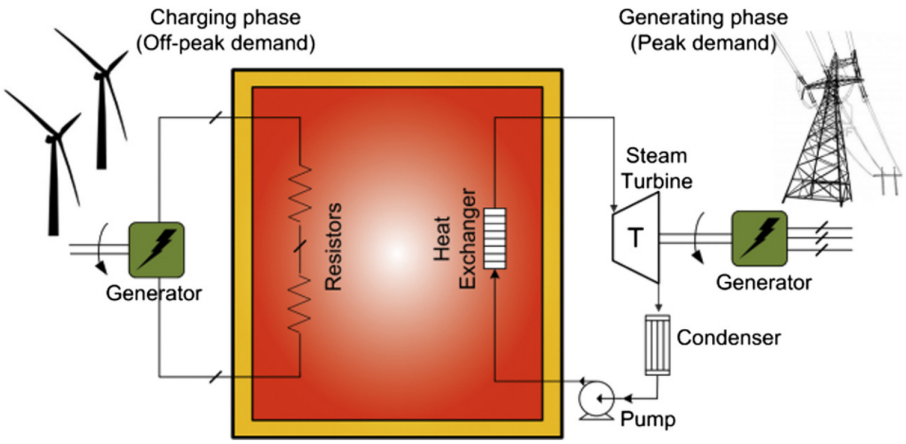

Figure 2.13: Layout of a TEES system using an electrical resistor during charge and the water/steam cycle during discharge. Diagram from: [6].

2.4.2 Proposed systems using ammonia or CO_2

Systems that pursue higher round-trip efficiencies must necessarily use a heat pump during charge. A system with these characteristics and which employs ammonia as working fluid has recently been proposed [9]. The cold reservoir uses the phase change between water and ice at 0 °C to drive the evaporation (charge) and condensation (discharge) of ammonia, while the hot reservoir is the environment. The scheme suffers from a very low temperature difference between both reservoirs. Since at least a few degrees of temperature between the working fluid and the reservoirs are required to drive the heat transfer, there is a big impact on the round-trip efficiency (see section 2.2.8). Additionally, the system uses an expansion valve rather than a liquid turbine for the expansion process of ammonia during the heat pump operation, posing a new source of exergy destruction. On the other hand, the same paper suggests using thermal energy from solar collectors to enhance the performance of the heat-engine, allowing a higher evaporation temperature during discharge (around 60 °C) and reaching top values of the round-trip efficiency of 84 %. Nevertheless, this apparently high value only considers the electricity as energy input, neglecting the extra energy obtained from the solar collectors. The authors justify this controversial decision because, in economic terms, there is no difference between a TEES system and a *solar-enhanced* TEES system (as long as the investment cost of the solar collectors is included), since the collection of the solar energy does not imply operating cost. However, one may argue that the same collectors could have a more efficient use if employed for water heating purposes elsewhere, or that if the same area was instead occupied with CSP collectors, more solar energy could be transformed into electricity by means of a water/steam cycle operating at a much higher temperature.

Another TEES system has been suggested based on a transcritical CO_2 cycle [8]. The pres-

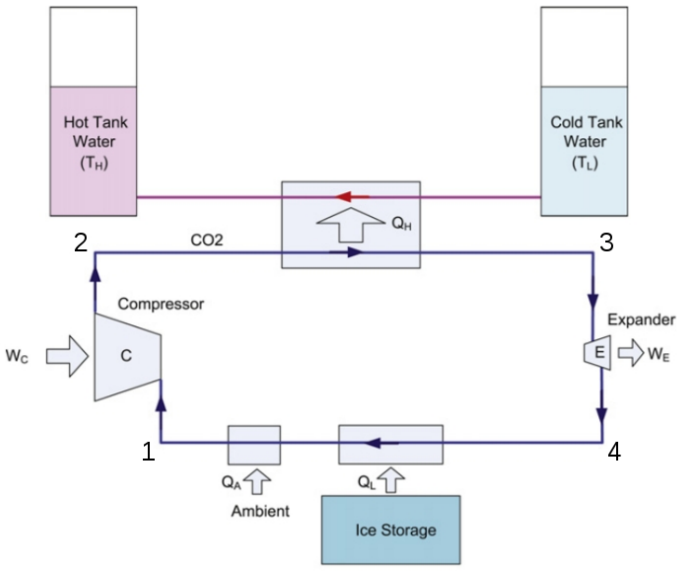

Figure 2.14: Layout of a TEES system based on the transcritical CO_2 cycle operating during charge [8].

sure at the high-pressure side of the cycle (between points 2 and 3 in Figure 2.12) is above the critical pressure, and this means that evaporation/condensation only happens when interacting with the cold reservoir (which consists again, of water/ice at 0 °C). This allows the heat exchange at the high pressure side to occur more efficiently, storing the thermal energy in the sensible heat of water by means of a counter-flow heat exchanger (see Figure 2.14). Even though the hot water tank is pressurized to allow a top water temperature of 120 °C, the temperature difference between the hot and the cold reservoirs continues to be relatively small. Another inconvenient of this scheme is that the specific heat capacity of CO_2 varies considerably over the specified temperature range, posing a pinch-point problem on the heat exchange between CO_2 and water (an equivalent problem which occurs between water and air at higher temperatures will be described in section 3.2). Using realistic values of compression and expansion isentropic efficiencies, and a minimum temperature difference for heat exchange, the authors obtain a round-trip efficiency of 60 %.

2.4.3 Potential of using the steam cycle both for charge and discharge

One may also try to design a TEES system similar to the one presented in Figure 2.13, but using the water/steam cycle in both directions, therefore replacing the electrical resistors for a heat pump. The main inconvenient of such a scheme is the extremely low pressure which is necessary to evaporate water at a temperature below ambient (0.017 bar at 15 °C). Such low pressures are not practical because of the high volumetric flow rates they involve. Even more important, running the cycle would become physically impossible as ambient temper-

ature approached 0 °C or below. It is necessary, therefore, to have a thermal energy source (a cold reservoir) lying at a higher temperature. Hong and Xin-shi describe the preparation of a compound Phase Change Material (PCM) using paraffin as a dispersed phase change substance and polyethylene as a supporting material [40]. The compound PCM undergoes phase change at around 60 °C and exhibits a heat of fusion of 155 $^{kJ}/_{kg}$ (i.e. around half the heat of fusion of ice). According to the authors, it is adequate for low-temperature heat storage applications because it is cheap, easy to prepare and can be directly contacted with a heat transfer medium. Additionally, it can be made of granular material with desirable dimensions and be used within a packed-bed for effective heat transfer. It would be possible, therefore, to transfer heat between the PCM and the evaporating/condensating water (at 0.2 bar around 60 °C, between points 4 and 1 in Figure 2.12) while maintaining a small temperature difference and keeping the exergy destruction to a minimum.

Performing efficient heat transfer at the high pressure side (between points 2 and 3 in Figure 2.12) shows an additional degree of complication. In order to avoid pinch-point problems, it is necessary to separately match the condensation/evaporation and the pre-heat and super-heat processes. The pressure of water can be adapted for condensation/evaporation to occur at the melting temperature of an adequate PCM. Several strategies are being currently investigated by different research groups for efficient steam generation using PCMs, particularly in the context of thermal energy storage for CSP plants [41]. These range from encapsulation of the PCM to embedding of heat exchanger pipes and heat transfer fins within the storage media. Another novel concept uses a Screw Heat Exchanger (SHE) to transport a salt (in this case, an eutectic mixture of $NaNO_3$ and KNO_3 with a melting point at 221 °C) at the same time that it exchanges heat with the working fluid [42]. A model of SHE is shown in Figure 2.15. This technology is particularly interesting because it allows to decouple the storage capacity and the heat transfer rate. Furthermore, both the pre-heating of water and the steam generation could be performed by employing two such SHEs and reusing the same PCM (first, using the sensible heat of the solid PCM, and then its latent heat). The same molten salt, once in the liquid form, could be used for the super-heating of steam through a more conventional counter-flow heat exchanger.

It should be noted that a TEES system like the one that is being discussed in this section could be implemented either independently or integrated to CSP plants that use water/steam as heat transfer fluid at the solar absorbers. In the latter case, it would allow the plants to both behave as facilities for energy production (from solar energy) and energy storage (from other energy sources). It seems reasonable that such a scheme could be particularly interesting for CSP plants located in regions far from the equator, where solar production is abundant during summer and scarce during winter, since the TEES system could allow the plant to increase the hours of operation during the worse months of the year.

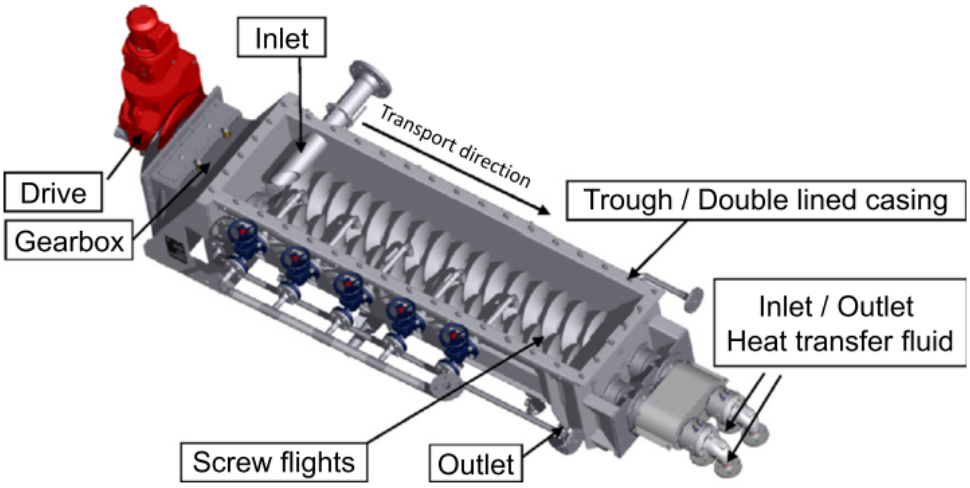

Figure 2.15: Detail of a Screw Heat Exchanger. A material can be transported and simultaneously heated/cooled by a heat transfer fluid. In the case of a PCM, it may enter as a fluid and leave as a solid or vice-versa [42].

2.4.4 Remarks

Section 2.4 has shown how several adaptations of the Rankine cycle are possible to design a TEES system. An advantage of the Rankine cycle in front of the JB cycle is the higher work ratio, which minimizes the effect of irreversibilities within compressors and expanders. On the other hand, attention has to be placed on avoiding pinch point problems and the associated exergy destruction.

To be able to make a fair comparison between all the various possible configurations (different working fluids, different sensible heat storage materials, different phase change materials...), it will be necessary to have a system model that can compute the different performance parameters of each cycle configuration. Such a system model will be composed of sub-models that represent the main components of the cycle, which is the topic of the next chapter.

Chapter 3

Component modelling

3.1 Goals and methods

The accuracy of the predictions performed by a model of a thermodynamic cycle depend on the accuracy of the sub-models that are used to describe the components of the cycle. A one-dimensional model of a heat exchanger is being developed and is presented in section 3.2. Some operational aspects of a reciprocating device have been briefly studied and are presented in 3.3.

Additionally, studies are being performed on two different aspects of packed-beds for thermal energy storage, from the perspective of Computational Fluid Dynamics (CFD). First, detailed CFD of packed-bed particles. Second, CFD of layered packed-bed stores. These are described in sections 3.4 and 3.5. These simulations are being carried with OpenFOAM, an open-source software based on C++ which is specialized on CFD.

3.2 Modelling of heat exchangers

Heat exchangers play an important role in thermodynamic cycles for energy storage. In those cycles that use solid materials as storage media (and direct heat transfer between the working fluid and the solid), they are used for waste heat rejection during discharge and for adjusting the fluid temperature at the exit of the thermal reservoirs. Additionally, in cycles that use liquid storage media, they are used to drive the heat transfer process between the working fluid and the storage liquid, and their performance largely influences the round-trip efficiency of the cycle.

Heat exchangers suffer from two main sources of exergy destruction. First, pressure losses due to shear stress and viscous dissipation. The impact of pressure losses on the overall system performance of a JB cycle was discussed in section 2.2.7. The second main source

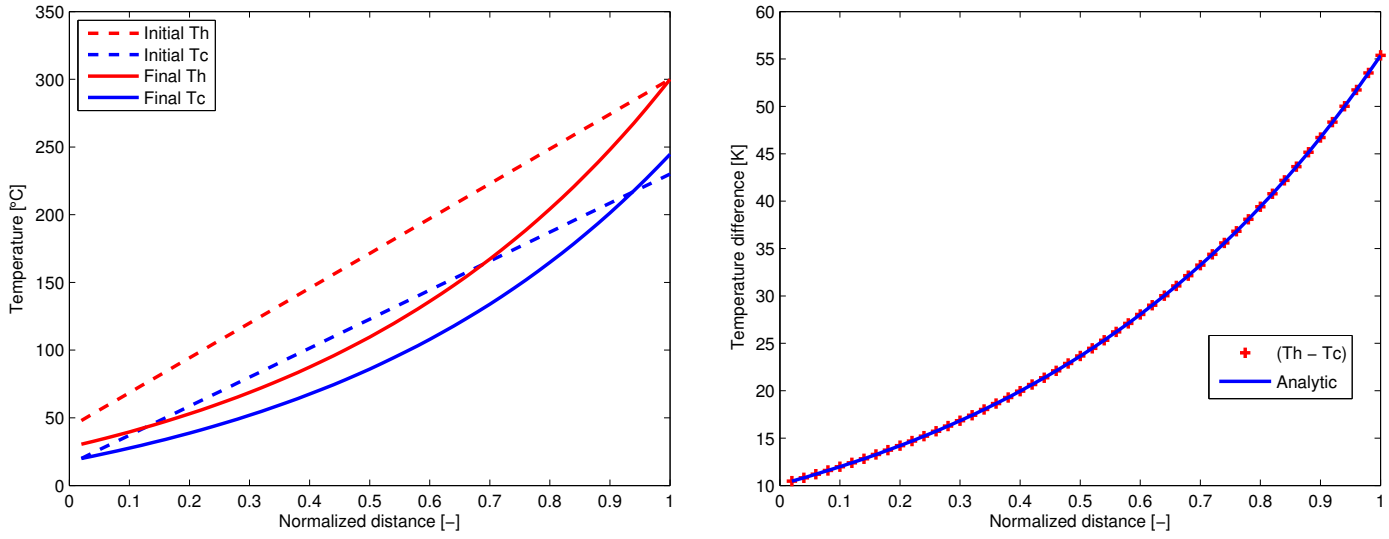

Figure 3.1: Left: Temperature distribution of the two fluids along the heat exchanger. Right: Comparison of the converged solution (red crosses) versus the analytical solution (blue line) of the temperature difference distribution.

of loss is heat transfer over a finite temperature difference, ΔT. Its impact on the performance of a generic TEES cycle was presented in section 2.2.8. It is interesting to investigate the limits on ΔT reduction and the relationship between ΔT and the pressure loss, among other performance parameters. This can be done through heat exchanger modelling, which is the subject of this section.

The type of heat exchanger most relevant to us is the counter-flow one, since its configuration allows to keep the hotter portions of the two fluids at one end and the colder portions at the other end [43]. This reduces the mean temperature difference between the two fluids and keeps the exergy destruction to a minimum.

An iterative code to compute the temperature distribution along such a exchanger was developed by Dr. Alex White. After setting an initial guess of the temperature over a number of heat exchanger sections, it iteratively adapts the distribution by applying the Steady Flow Energy Equation at each section, until reaching convergence. The code considers a given overall heat transfer coefficient, U, and assumes that the thermophysical properties of the two fluids (and particularly their specific heat capacities, $c_{p,h}$ and $c_{p,c}$) are constant over the relevant temperature range.

Figure 3.1 shows the temperature distribution of the two fluids for a given set of input parameters (U, $c_{p,h}$ and $c_{p,c}$, inlet temperatures, mass flow rates and total heat transfer surface). The cold fluid (in blue) enters at 0 and leaves at 1, while the hot fluid (in red) enters at 1 and leaves at 0. Dashed lines indicate the initial guess of the simulation before iteration

starts. The solid lines show the converged solution. In the given example, the *heat capacity rate*, $\dot{m}c_p$, of the cold fluid was bigger than the one of the hot fluid, and this explains the smallest temperature difference between both fluids to happen at the cold inlet. The assumption of constant $c_{p,h}$ and $c_{p,c}$ allows the solution of the simulation to be compared with the analytical solution of the problem, which can be found in general heat transfer textbooks [44]. This is shown at the right hand side of the same figure.

The author of this report is currently extending the mentioned code to account for varying thermophysical properties and consider geometrical parameters that allow the computation of U and of the pressure losses according to the given operating conditions (temperature, pressure, mass flow rate). The first step is setting a library that contains the thermophysical properties of the fluids that will be used in the simulations. A cross-platform, open-source thermophysical properties library, named CoolProp, contains data on more than a hundred fluids [45]. It will be used as a main source of information for treating working fluids such as air, argon, steam, ammonia, ethanol or carbon dioxide. Nevertheless, the library does not contain information on most of the fluids that have been suggested in this report to be used as media for thermal energy storage (see Table 2.1), such as molten salts, thermal oils or molten metals. Instead of CoolProp, the literature referenced in section 2.3.1 (among others) will be used for that purpose.

Data files containing tables of thermophysical properties are being created. As a first step, tables containing the value of c_p as a function of T (with spacings of 5 K between data points) have been prepared. At execution, the program imports the data from the external files and stores it in matrices. Then, the temperature distribution set by the initial guess is used to create a *heat capacity distribution* by interpolating the values from the matrices. Since the temperature distribution evolves as the iterative process continues, it is necessary to update the c_p distribution. Nevertheless, reading and interpolating from the matrices is relatively slow, and one would try to avoid doing this operation at each iteration. Instead, it has been found that updating the c_p values only every 10 to 20 iterations maintains convergence stability while keeping computational expenses to a minimum.

Figure 3.2 presents the results of two simulations using the thermophysical properties capability. In both cases, air at 1 bar is the hot fluid and water at 200 bar is the cold fluid. In both simulations, water enters the heat exchanger at 20 °C through the cold inlet, and its mass flow rate is adapted so that the average heat capacity rates of both fluids are the same. In one simulation, though, air enters the hot inlet at 300 °C, while in the other it does so at 365 °C. The difference of doing so is substantial, as can be seen by comparing the upper T-Q diagrams of the mentioned figure. In the first case the maximum temperature difference between fluids is around 10 K, while on the second one it reaches 45 K next to the cold inlet (see the bottom-left diagram). This effect can be understood by comparing the

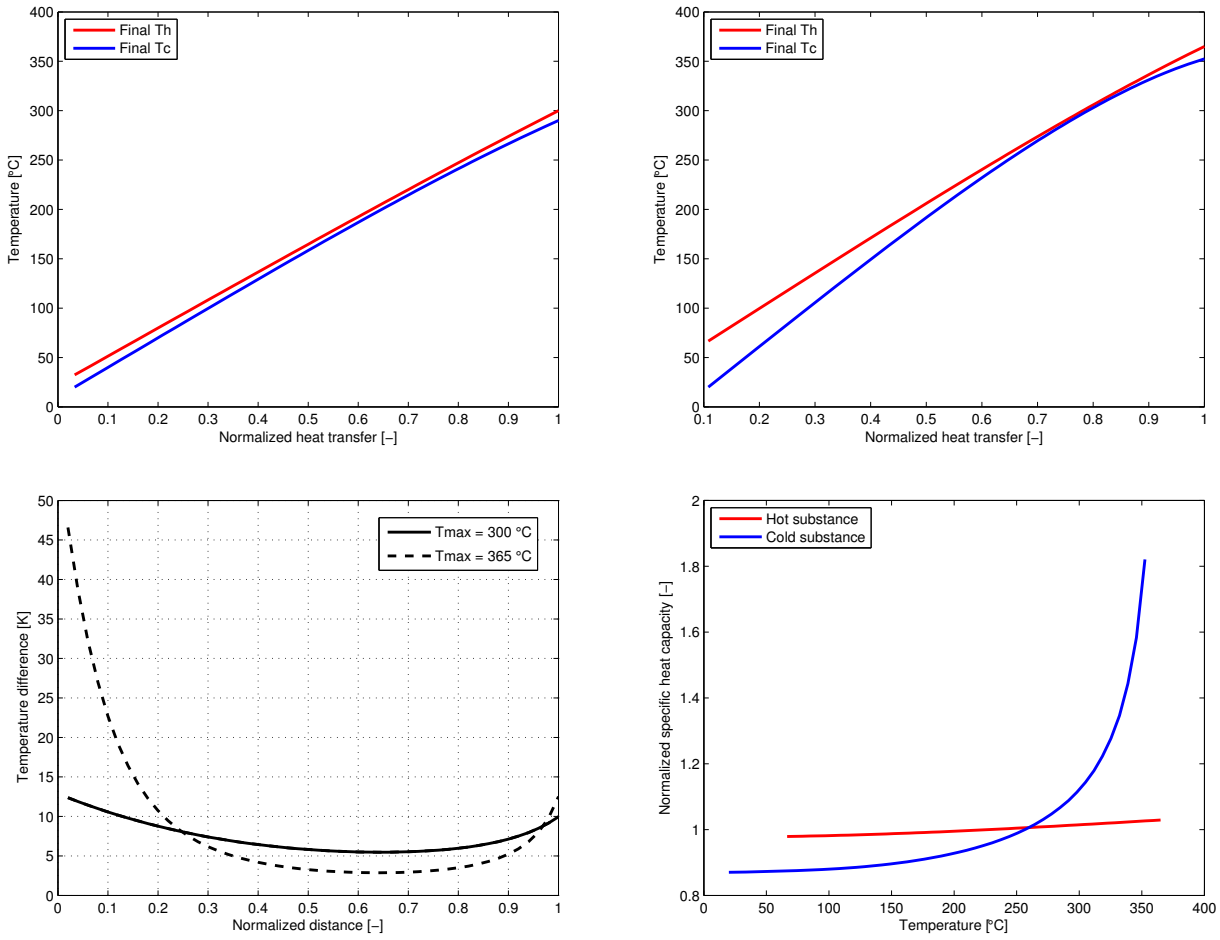

Figure 3.2: Above: T-Q diagrams obtained by simulation of a heat exchanger, with air and pressurized water as hot and cold fluids, respectively. On the top-left diagram, air enters at 300 °C, while on the top-right it does so at 365 °C. Bottom-left: distribution of ΔT for both simulations. Bottom-right: comparison of the (normalized) c_p values of both fluids over the relevant temperature range.

evolution of c_p with T for both fluids, as shown in the bottom-right diagram (where c_p has been normalized by its average in each case). The c_p of air is practically constant over the relevant temperature range in both cases. Nevertheless, while the c_p of water (at 200 bar) does not change significantly until 250 °C, it shows a sharp increase after 300 °C as it starts to approach the critical temperature. This effect creates large variations of the heat capacity rate distribution, establishing a pinch point and increasing the mean temperature difference between the fluids. This is of course a negative effect, as it increases the exergy destruction and limits the amount of work that a hypothetical TEES system using such a exchanger could recover.

Having a heat exchanger model that considers varying thermophysical properties is therefore a critical step towards system modelling of TEES systems with liquid reservoirs. Further extension of the code that is currently being performed includes the selection of geometrical parameters that allow the calculation of the Reynolds number, and the use of correlations to obtain the Nusselt number and the pressure drop from it. Further results will be available soon.

3.3 Modelling of reciprocating devices

As mentioned earlier, reciprocating compressors and expanders are receiving attention by various research groups because of their potentially higher polytropic efficiencies than turbomachines. In particular, Dr. Caroline Willich, from our group at CUED, is performing CFD simulations of gas springs to investigate the effects of complex heat transfer between the gas and the cylinder walls, which is a major source of loss. Another aspect that is worth investigating is how the mass flow rate and the pressure ratio can be adapted and if it is possible to do so independently from each other and from the driving frequency.

Consider the Compressed Air Energy Storage (CAES) system in Figure 3.3, which consists of two different compressors and two different TES devices. Air is compressed, cooled, compressed again and cooled again before entering a cavern. Energy is separately stored in the form of a pressure potential between the inside and the outside of the cavern and in the form of sensible heat in the TES reservoirs. As the pressure inside the cavern increases, the second compressor must increase its pressure ratio accordingly, and ideally it should be able to do so without changing the mass flow rate. Dr. Willich and the author of this report investigated how this could be done by setting a loss-free model of a reciprocating compressor, using the MATLAB language and programming environment. The model is presented below.

A p-V diagram of the four idealized stages of the compressor is presented in the top-left part of Figure 3.4. They are the following: (a) Isentropic compression $1 \rightarrow 2$ (valve off). (b) Isobaric expulsion $2 \rightarrow 3$ (valve on). (c) Isentropic expansion $3 \rightarrow 4$ (via 3b, valve off). (d)

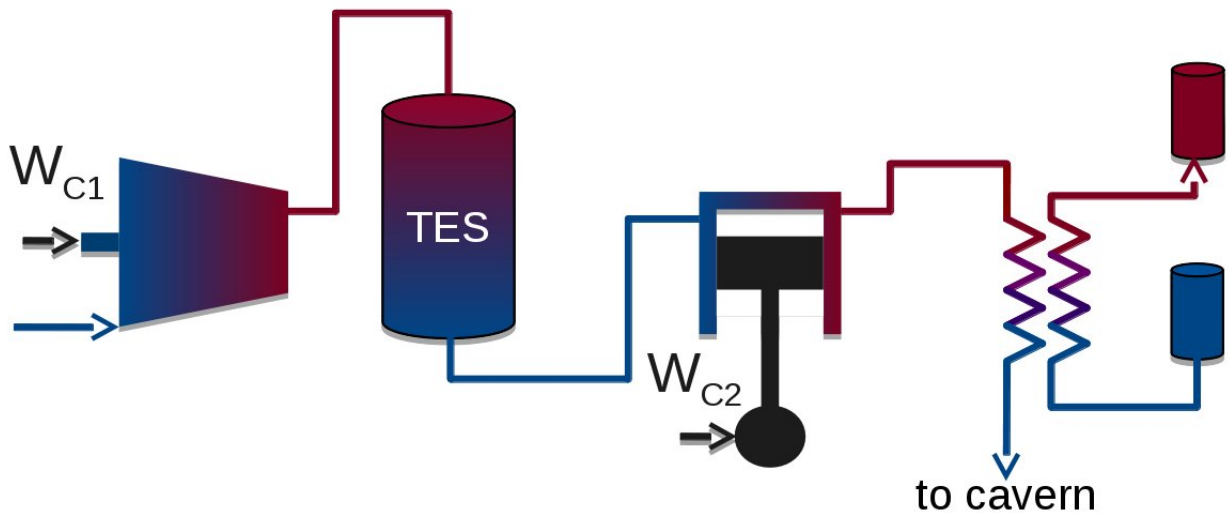

Figure 3.3: Possible configuration of a CAES system using two different compressors and two different TES systems. Adapted from: [13]

Isobaric expulsion 4 $\rightarrow$ 5 (valve on). Typically, the valve at 3 would be turned off exactly at Top Dead Centre (TDC) and the path between 3 and 3b would disappear. The same would happen to the path between 5 and 1 at Bottom Dead Centre (BDC). Nevertheless, it is actually the effect of changing the valve timings that we are interested on.

The crank angles corresponding to 3b and 1 are fixed, since they represent TDC and BDC. Additionally, the crank angle at 4 (CA4) may vary, but it is not selected as an input since the valve simply opens when the pressure reaches the value of the inlet pressure, p_{inlet}, at the end of the expansion stage. Therefore, there are three events that we may modify: the opening of the valve at the end of the compression stage (at crank angle 2 - CA2), the closure of the valve after expulsion (CA3) and the closure of the valve after suction (CA5). p-V diagrams showing these variations are also shown in Figure 3.4.

We notice that delaying the aperture of CA2 increases the pressure ratio (since p_{outlet} increases) and diminishes the mass flow (this can be easily seen from the reduction in the volume swept by the cylinder during suction, between points 4 and 5). Similarly, advancing the closure of CA3 also reduces the mass flow, although it has no impact on the pressure ratio (since the valve at CA4 adapts its timing to the inlet pressure). Advancing the closure of CA5 alone, however, reduces both the mass flow and the pressure ratio. Combinations are also possible. For example, by advancing CA5 and delaying CA2 it is possible to keep the pressure ratio constant while only diminishing the mass flow, similarly to what happens when changing CA3. The previous discussion may be evaluated in more detail by examining the first four diagrams of Figure 3.5. Finally, the last two diagrams of the same figure show

curves of the pressure ratio as a function of the mass flow.

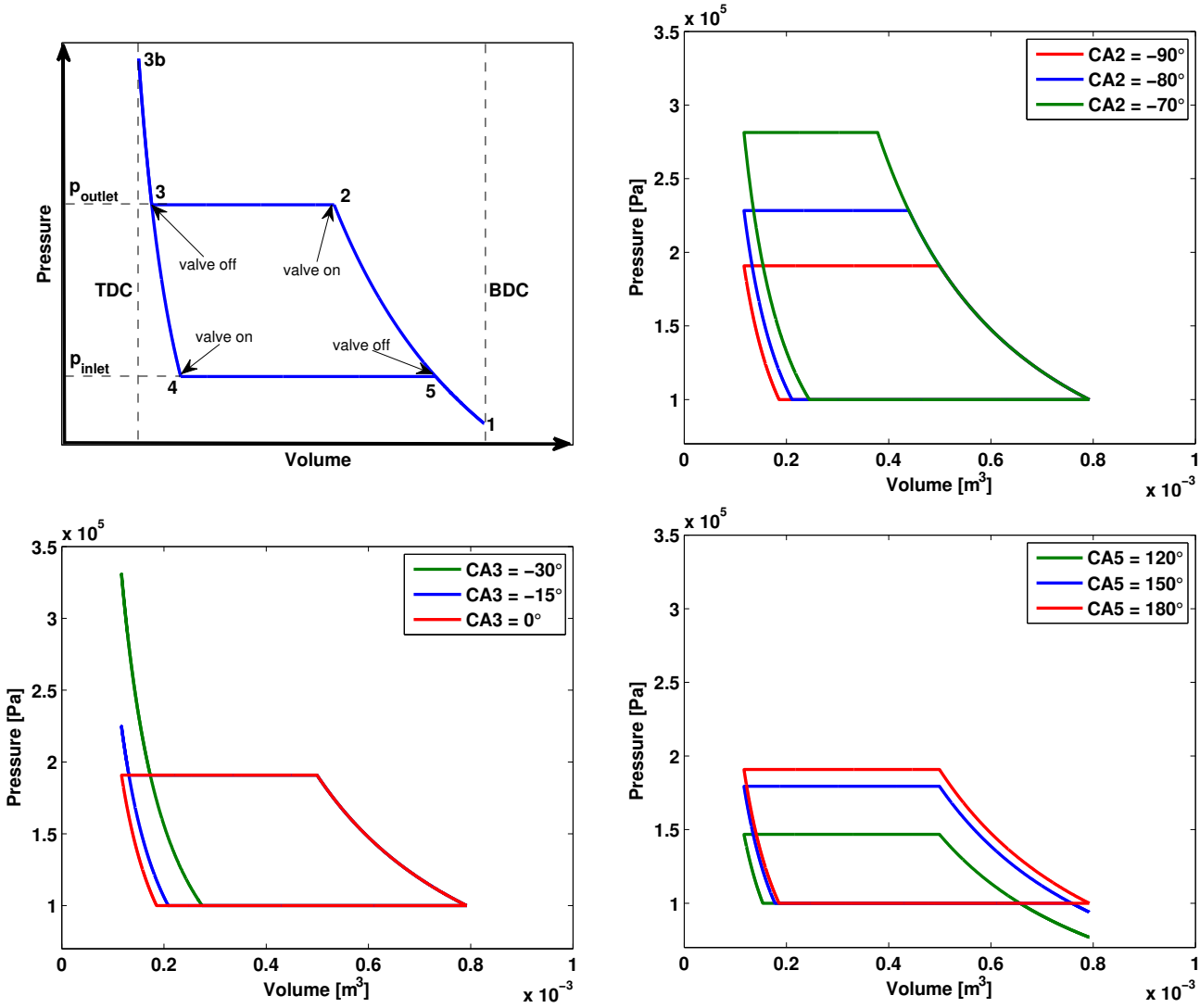

Figure 3.4: Top-left: Idealized p-V diagram of a reciprocating compressor. BDC and TDC indicate the volume lines at Bottom Dead Centre and Top Dead Centre, respectively. The other three diagrams show the impact of changing the valve timings corresponding to points 2 (top-right), 3 (bottom-left) and 5 (bottom-right).

We may conclude that by varying the timing of the valves we can adapt the pressure ratio and mass flow delivered by a reciprocating compressor to our needs. For example, we can increase the pressure ratio while keeping the mass flow constant, which is a useful feature for some CAES systems. The same results are easily reproducible for a reciprocating expander, as only the flow direction and the valve timings are modified. Nevertheless, this simplified model has so far ignored the irreversible processes that in reality occur during the four stages of the cycle. The impact that adapting the valve timings has on such losses should be investigated to find the practical limitations of this method.

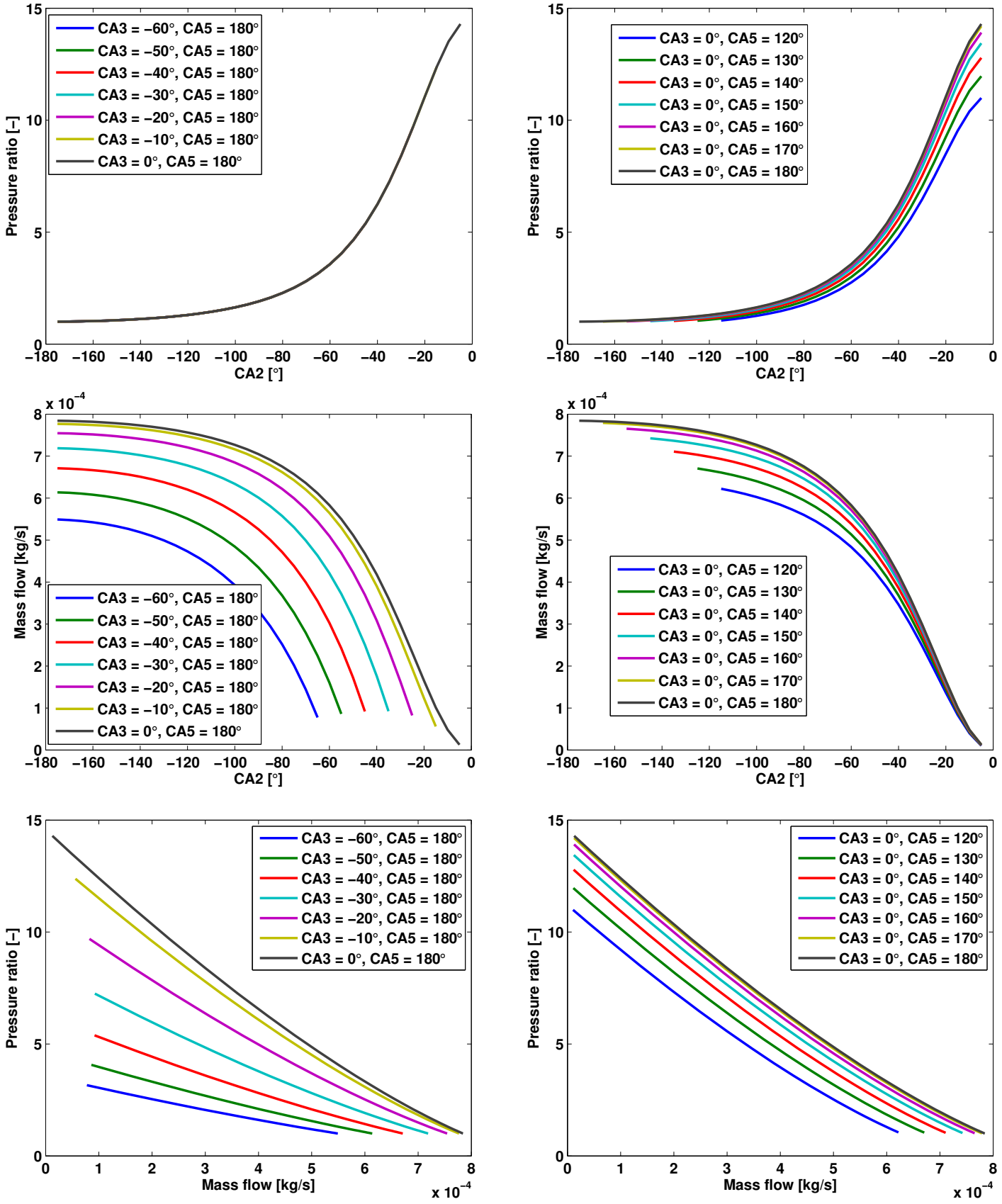

Figure 3.5: Effects of varying CA3 and CA5. Top: pressure ratio as a function of CA2. Middle: mass flow as a function of CA2. Bottom: pressure ratio as a function of mass flow.

3.4 CFD of packed-bed particles

Two main sources of loss in packed-bed thermal reservoirs are pressure loss and irreversible heat transfer through the finite temperature difference between gas and solid. In order to accurately predict these losses and try to minimize their combined effect, it is necessary to understand how they vary according to relevant parameters like the flow speed or the particle size, shape and distribution within the bed. Selecting the proper heat transfer correlation has a critical result on predicting losses and the evolution of the thermal fronts, as was found in [46]. Nevertheless, there is significant spread of the values obtained by various correlations from the literature on packed-bed, and it is interesting to better understand the factors influencing these differences.

The final aim here is to perform 3D simulations of flow and heat transfer between a gas and a finite number of solid particles, resembling the conditions inside packed-bed thermal reservoirs. Ultimately, the effect of varying configuration and particle shape should be studied, as well as the impact of varying thermophysical properties. Nevertheless, before performing any complex CFD simulation, it is important to test the solver and the methodology with simpler test cases that can be compared with existing experimental data or analytical results. Following such a process thoroughly is particularly important when the person performing the study is new to the CFD field, as was the author of this report at the beginning of the project. The initial test case used for validation purposes is therefore much more simple than the final aim. It consists on simulation of flow around a single 2-dimensional particle, i.e. effectively flow around a circular cylinder.

The mesh that was used for this test case is presented in Figure 3.6. It was created using blockMesh, an OpenFOAM utility to generate structured meshes. The mesh was refined towards the surface of the cylinder, where low aspect-ratio cells are used. It also presents a denser grid at the back of the cylinder (the flow direction is in the positive x-axis direction), to better capture the flow and temperature gradients that propagate in that region. A mesh refinement study was performed to ensure that the mesh resolution was adequate and that the solution was no longer dependent on increasing or decreasing number of cells.

Two different OpenFOAM solvers [47] have been used to compute this test case:

icoFoam *Transient solver for incompressible, laminar flow.*

simpleFoam *Steady-state solver for incompressible, turbulent flow.*

Despite the description of simpleFoam stating that it is a solver for turbulent flow, it can also be used to resolve laminar simulations by setting its turbulence model to laminar. Otherwise, the default RANS $k - \epsilon$ model may be used.

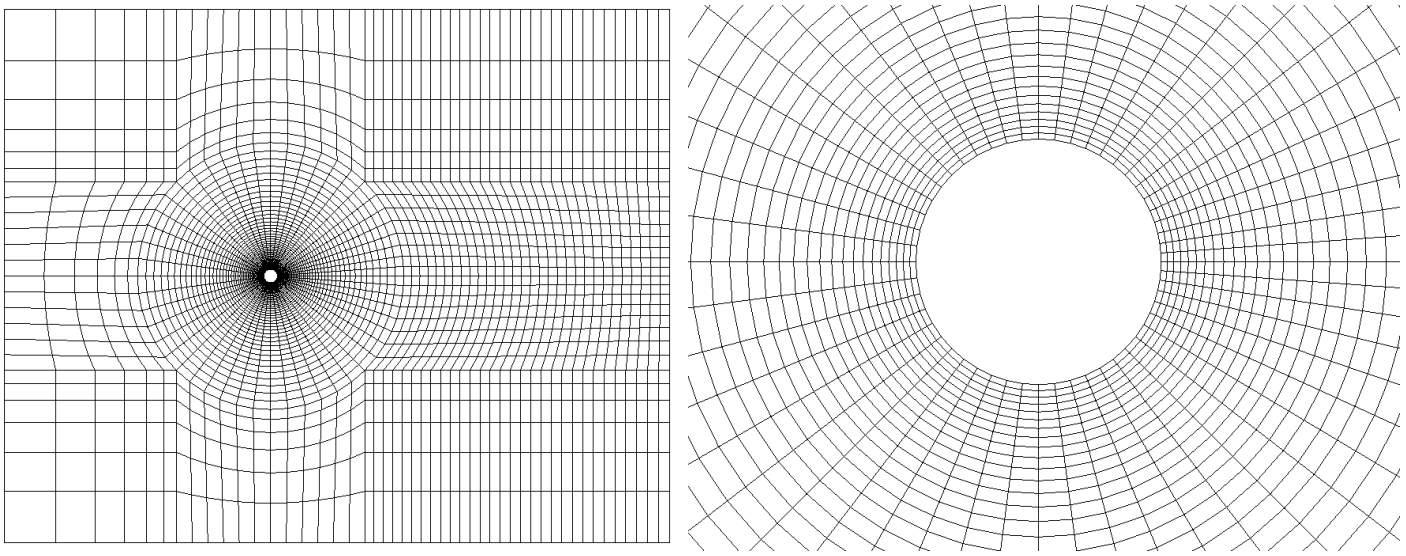

Figure 3.6: Grid used for simulation of flow around a cylinder.

Apart from visualizing the flow patterns that are generated around the object of study, the aim is to reproduce two specific correlations: the variation of drag coefficient and Nusselt number with the Reynolds number, $C_d\,(\mathrm{Re})$ and $\mathrm{Nu}\,(\mathrm{Re})$, respectively. Methodology and results are presented below.

3.4.1 Variation of drag with Reynolds number

The first solver to be tested is icoFoam. As a transient solver for incompressible flow, it solves the momentum equation in the following form:

$$\frac{\partial \vec{u}}{\partial t} + \vec{u}\,\vec{\nabla}\vec{u} - \nu\,\nabla^2\vec{u} = -\vec{\nabla}p_\rho$$

where $\vec{u}$ is the velocity vector field (in $^{\mathrm{m}}/_{\mathrm{s}}$), $\nu \equiv {}^{\mu}/_{\rho}$ is the *kinematic* viscosity (in $^{\mathrm{m}^2}/_{\mathrm{s}}$) and $p_\rho \equiv {}^{p}/_{\rho}$ represents a *kinematic* pressure and has units of $^{\mathrm{m}^2}/_{\mathrm{s}^2}$. The other symbols have their usual meaning, i.e. ${}^{\partial}/_{\partial t}$ is the partial derivative with respect to time, $\vec{\nabla}$ is the nabla operator and $\nabla^2 = \vec{\nabla}\cdot\vec{\nabla}$.

The aim is to make the solver run and extract results when a steady state solution has been reached. The boundary conditions are as following: a fixed velocity is set at the left boundary (inlet), which will be varied to obtain different values of the Reynolds number. A fixed kinematic pressure is set at the right boundary (outlet). The upper and lower boundaries are set as symmetry planes.

The Reynolds number is calculated by:

$$\mathrm{Re} = \frac{u_\infty\, d_c}{\nu} \tag{3.1}$$

where u_∞ is the free-stream velocity (in this case, the velocity at the inlet) and d_c the diameter of the cylinder.

The drag coefficient is calculated by:

$$C_d = \frac{F_d\, p}{\frac{1}{2\pi}\,\rho\, A_c\, u_\infty} \tag{3.2}$$

where F_d is the drag force, and A_c is the side area of the cylinder. Even if the geometry is 2-dimensional, OpenFOAM always works with 3 dimensions and in this case this is done by setting a single layer of cells of an arbitrary length in the z direction (inside the plane). Therefore A_c has still units of m^2. A_c/π gives the projected area of the cylinder orthogonal to the direction of the flow. F_d is obtained by adding the x-components of the pressure force $\vec{F}_p$ and the viscous stress $\vec{F}_\mu$ on the cylinder surface:

$$F_d = \left(\vec{F}_p + \vec{F}_\mu\right)_x$$

with

$$\vec{F}_p = -\rho\,\mathrm{int}(p\,\vec{n}\;\, d\,A)_{A_c}$$

$$\vec{F}_\mu = \rho\,\nu\,\mathrm{int}\left(\vec{\nabla}_{\vec{n}}\,\vec{u}\;\, d\,A\right)_{A_c}$$

where p is the pressure acting on a infinitesimal element of area dA and $\vec{n}$ is the unit vector that provides the direction of dA. $\vec{\nabla}_{\vec{n}}$ represents the gradient normal to the surface, and the $\mathrm{int}\,()$ function represents an integral, in this case around A_c. In practice, dA represents the surface of a cell face on the cylinder patch and the integral is substituted by a discrete summation on all the cell faces that cover A_c. Application of these expressions allows us to obtain data points of the correlation $C_d\,(\mathrm{Re})$. Figure 3.7 presents the results obtained with the two different solvers, icoFoam and simpleFoam. Data points extracted from an experimental curve presented in [48] are used for comparison and validation, together with the plot of a theoretical correlation which is valid in the limit of low Reynolds numbers [49]:

$$C_d = \frac{8\pi}{\mathrm{Re}\,(2.002 - \ln \mathrm{Re})}$$

The values obtained with both solvers are close to the theoretical and experimental results, with icoFoam performing slightly better than simpleFoam at low Re, and the opposite for higher Re. The advantage of using simpleFoam is that, being a steady-state solver, it reaches convergence much faster than icoFoam. On the other hand, icoFoam is able to capture temporal physical features that are lost when using a steady-state solver like simpleFoam. Particularly, for values above $\mathrm{Re} \sim 60$, oscillating vortices start to appear at the back

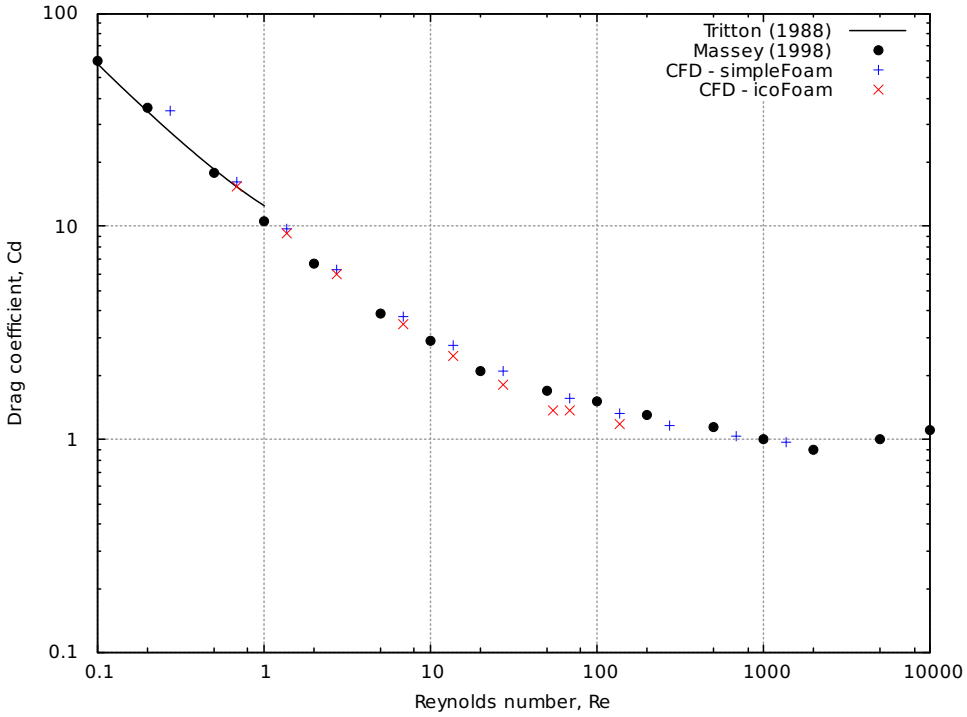

Figure 3.7: Correlation of $C_d\,(\mathrm{Re})$ for an infinitely long circular cylinder. Results from CFD simulations together with the analytical solution for creep flow (black line) and experimental data (black dots).

of the cylinder. The vortices move up and down in a manner that the flow is instantaneously unsteady but globally periodic. icoFoam reproduces this unsteady situation as shown in Figure 3.8, where the steady-state solution reached for $\mathrm{Re} = 27$ is contrasted to a snapshot of the unsteady solution for $\mathrm{Re} = 68$. Once in the unsteady regime, the drag coefficient oscillates and has to be averaged over time. This was the procedure followed for the last two data points generated with icoFoam that appear in Figure 3.7. For higher Reynolds numbers, the flow becomes too turbulent and attempts to continue using icoFoam were unsuccessful, as computation became unstable. Even if at the cost of a slightly less physically accurate solution, using simpleFoam it was possible to proceed towards higher Re values, accurately predicting the values of the drag coefficient up to $\mathrm{Re} \sim 1000$ and above.

3.4.2 Variation of heat transfer with Reynolds number

After verifying that the selected solvers satisfactorily reproduce the $C_f\,(\mathrm{Re})$ correlation on the circular cylinder, the next step is introducing heat transfer. icoFoam and simpleFoam are solvers for incompressible flow that are not specialized on heat transfer simulations. As such, they do not need to solve the energy equation and they restrict themselves to solving the momentum equation. Indeed, temperature does not even appear as a property of the flow

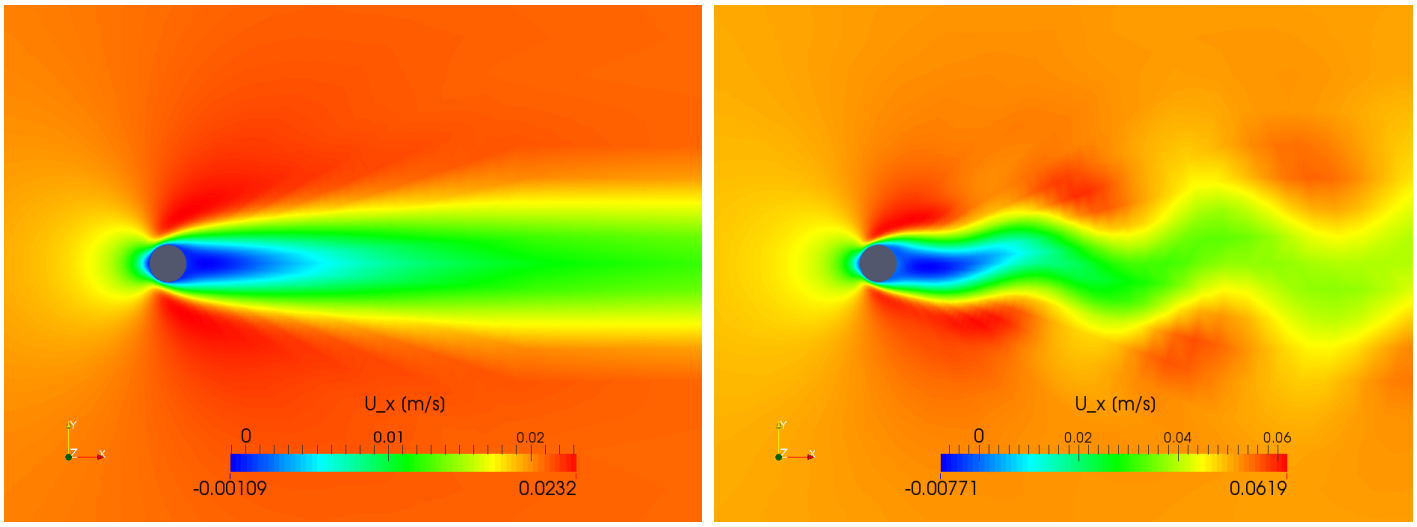

Figure 3.8: Horizontal component of the velocity field generated by icoFoam at two different Reynolds numbers. Left: Re = 27 (steady-state). Right: Re = 68 (snap-shot of the unsteady flow).

field. Following an OpenFOAM tutorial [50], the new field was included and an equation to describe the transport of temperature was coded into the two solvers, as following:

$$\frac{\partial T}{\partial t} + \vec{u}\,\vec{\nabla} T - \alpha\,\nabla^2 T = 0$$

with

$$\alpha \equiv \frac{\kappa}{\rho\, c_p}$$

where α is the thermal diffusivity (m^2/s) and κ the thermal conductivity of the fluid ($\mathrm{W}/(\mathrm{m\,K})$). Since this expression simply describes the propagation of an additional and independent property (in this case the temperature field), it has no impact on the momentum equation and does not change the flow characteristics of the previous solutions. This is not generally true, as temperature changes imply changes in density and in the transport properties, that at their turn affect the pressure and velocity fields. To be strict when working with heat transfer, one would need to use a compressible solver and varying thermophysical properties. Therefore, it is necessary to recognize that the validity of results obtained with this method is restricted to scenarios with relatively small temperature changes. Nevertheless, the approximation is good enough for our current purposes. Figure 3.9 shows the propagation of the temperature field for Re = 27 when setting the cylinder temperature at 300 K, the flow temperature at 288 K, and constant values for the kinematic viscosity and thermal diffusivity that roughly correspond to those of air at 288 K.

The interest at this point is to obtain the values of the Nusselt number at different Reyn-

olds numbers, Nu (Re). The Nusselt number is:

$$\mathrm{Nu} = \frac{h\, d_c}{\kappa} \tag{3.3}$$

where

$$h = \frac{\dot{q}_c}{A_c\,(T_c - T_\infty)} \tag{3.4}$$

Note that in this context h represents the heat transfer coefficient ($\mathrm{W}/(\mathrm{m}^2\,\mathrm{K})$) rather than the enthalpy, as it did in previous chapters. $\dot{q}_c$ is the heat transfer rate from the cylinder to the fluid (W), T_c is the surface-averaged temperature of the cylinder wall and T_∞ the free-stream temperature (in practice, the temperature set at the inlet boundary condition). The heat is first transferred between the solid and the fluid by conduction (as thermal radiation is being neglected at this point) and then transported by conduction and convection. Conduction at the cylinder wall is computed with the integral:

$$\dot{q}_c = -\kappa\,\mathrm{int}\Big(\vec{\nabla}_{\vec{n}} T\ \, dA\Big)_{A_c} \tag{3.5}$$

The global heat transfer coefficient and the Nusselt number are readily calculated by implementation of the previous expressions. By removing the integral in (3.5), we may also obtain the *local* values of the heat transfer coefficient, which can be expressed, for instance, as a function of the angular position around the cylinder, θ:

$$h(\theta) = \frac{\dot{q}(\theta)}{A(\theta)(T(\theta) - T_\infty)}$$

$$\dot{q}(\theta) = -\kappa\,\vec{\nabla}_{\vec{n}} T(\theta)\, dA(\theta)$$

The *local* heat transfer coefficient has been plot in Figure 3.9 according to two different boundary conditions: constant temperature and constant heat transfer rate, which are set as constraints on the temperature field at the surface of the cylinder. To be able to make a meaningful comparison between the two situations, the global heat transfer rate, $\dot{q}_c$, was set to be the same. This was done by first running each simulation with the constant temperature condition (i.e. $T(\theta) = 300\,\mathrm{K}$), computing the value of $\dot{q}_c$ when the steady-state solution was reached, and then using this value to impose the constant heat transfer condition for the second set of the simulations. This is done through a constant surface-normal temperature gradient condition, as following:

$$\vec{\nabla}_{\vec{n}} T(\theta) = \frac{-\dot{q}_c}{A_c \kappa}$$

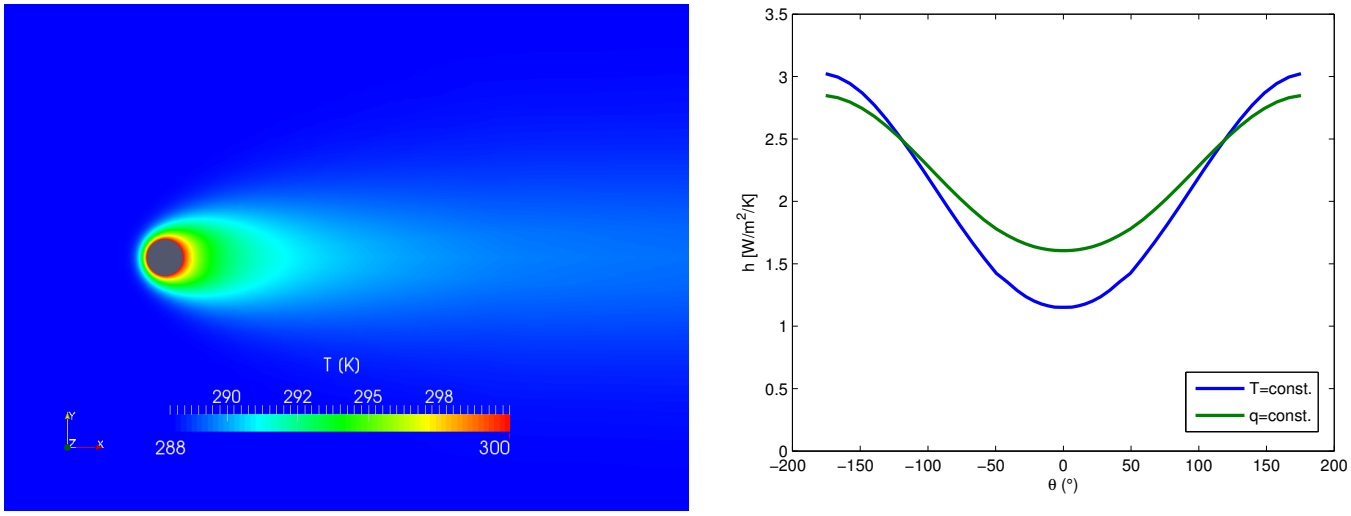

Figure 3.9: Left: propagation of the temperature field at Re = 27. Right: variation of the local heat transfer coefficient along the cylinder surface for two different boundary conditions, constant temperature and constant heat transfer.

The procedure was repeated for various values of the Reynolds number and using the adapted version of the two solvers, icoFoam and simpleFoam. The steady state condition for each simulation was validated with mass, momentum and energy conservation checks between the external boundaries of the mesh and the cylinder surface. As explained in the previous section, oscillating vortices appear at the back of the cylinder when using icoFoam at high values of Re, and time average has to be performed when this happens. Results are presented in Figure 3.10, together with three different correlations extracted from the literature. The correlations from Fand (1965) and Whitaker (1972) were obtained from a short compilation presented in [51]. A more modern correlation, Sparrow (2004), was obtained from [52]. While the three correlations converge as they move into the high Re regime, they separate substantially from each other at the low Re end. Most correlations encountered in the literature refer to flow in the high Re regime, and according to [51], the correlation from Fand (1965) is the only one (from those compiled) which is applicable at values of Re < 1. This may explain the better agreement between the CFD results and that correlation in the low Re regime. Differences between the results obtained by the two solvers are practicably negligible. The small differences obtained when applying the two different boundary conditions are also difficult to observe in the log-log scale; note that despite the noticeable changes on the distribution of the local heat transfer coefficient along the cylinder surface (shown in Figure 3.9), the average values for the two conditions remain close to each other. Finally, a divergence appears between the data points obtained with simpleFoam and the three literature correlations as we advance into the high Re regime. This could be because of an inadequate

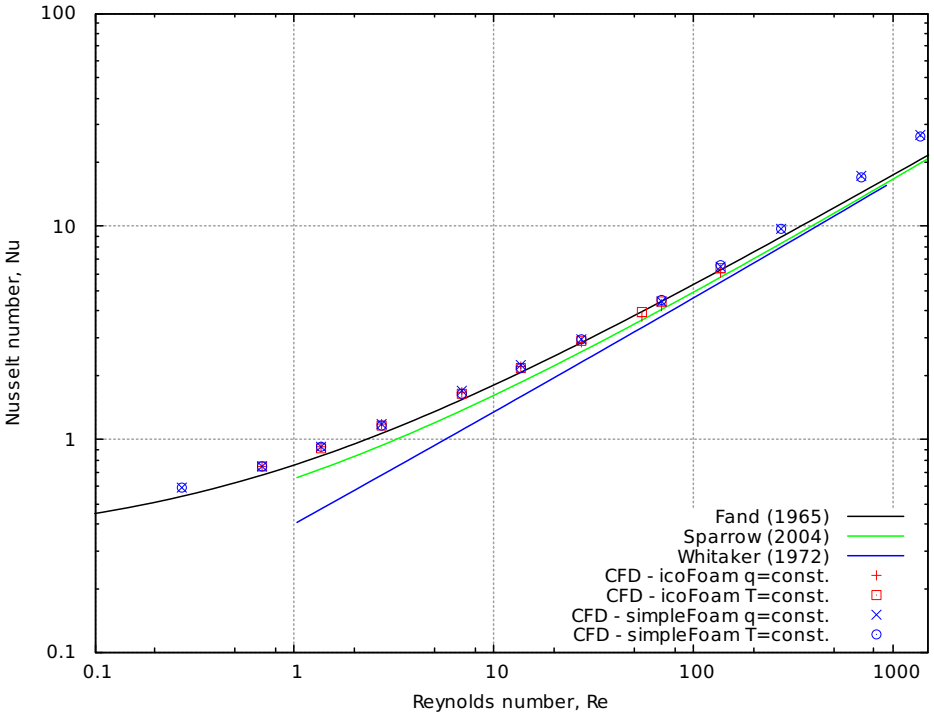

Figure 3.10: Correlation of Nu(Re) for an infinitely long circular cylinder. Results from CFD simulations together with correlations extracted from literature.

setting of the turbulence model and should be carefully inspected. Once the cause of this divergence is understood and corrected, the initial validation stage will have concluded satisfactorily and it will be possible to proceed with simulations of more complex geometries, as explained at the beginning of this section.

3.5 CFD of layered packed-bed thermal reservoirs

The direct heat transfer process between the working fluid and the solid particles of a packed-bed creates a thermal front that advances through the reservoir. The finite temperature difference between gas and solid, as well as conduction within the bed, leads to the deterioration of the thermal front, which starts spreading as a wider gradient through the reservoir. This process limits the energy density of the system, as the energy stored within the gradient cannot be recovered efficiently. It would be interesting, therefore, to keep the region of the thermal gradients as thin as possible. This can be achieved by decreasing the size of the solid particles, which increases the contact surface area and reduces the temperature difference between gas and solid. Nevertheless, doing so has the disadvantage of also increasing the pressure loss.

Dividing the thermal reservoirs in several layers of smaller particles has been suggested

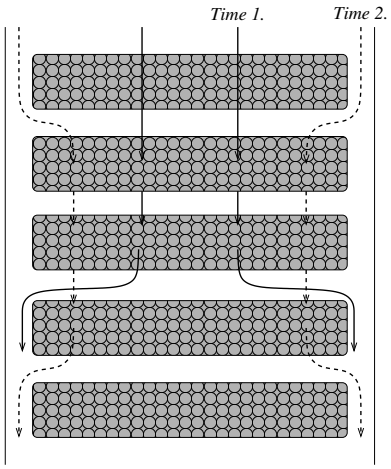

Figure 3.11: Layout of a segmented store, showing the paths followed by the gas through the packed-bed layers at two different points in time. Picture from: [53].

as a way to reduce the size of the thermal gradient while simultaneously keeping the pressure loss down [53]. A valve mechanism makes the gas go through a reduced number of layers that are being charged and skip the inactive layers, as shown in Figure 3.11. The magnitude of the pressure loss associated with the valve mechanism, however, is not yet clear and will be investigated via CFD simulation.

Porous media can be modelled by adding a pressure sink term to the momentum equation [54]. Two porosity models are available in OpenFOAM. The first one computes the pressure loss using a power law of the velocity:

$$\frac{\partial p}{\partial x_i} = -\rho C_0 |u_i|^{(C_1-1)/2}$$

where C_0 and C_1 are empirical coefficients. The second one uses the Darcy-Forchheimer model, which divides the pressure loss into two different contributions, a *viscous* term and an *inertial* term:

$$\frac{\partial p}{\partial x_i} = -\left(\frac{\mu}{K} + b\rho|\vec{u}|\right) u_i \tag{3.6}$$

where the *permeability* K (in m^2) and the coefficient b (in m^{-1}) must again be obtained from empirical correlations. For a column of packed spheres, Bejan [55] suggests using the Ergun's correlations, according to which:

$$\begin{aligned} K &= \frac{d_p^2 \varepsilon^3}{150(1-\varepsilon)^2} \\ b &= \frac{1.75(1-\varepsilon)}{d_p \varepsilon^3} \end{aligned} \tag{3.7}$$

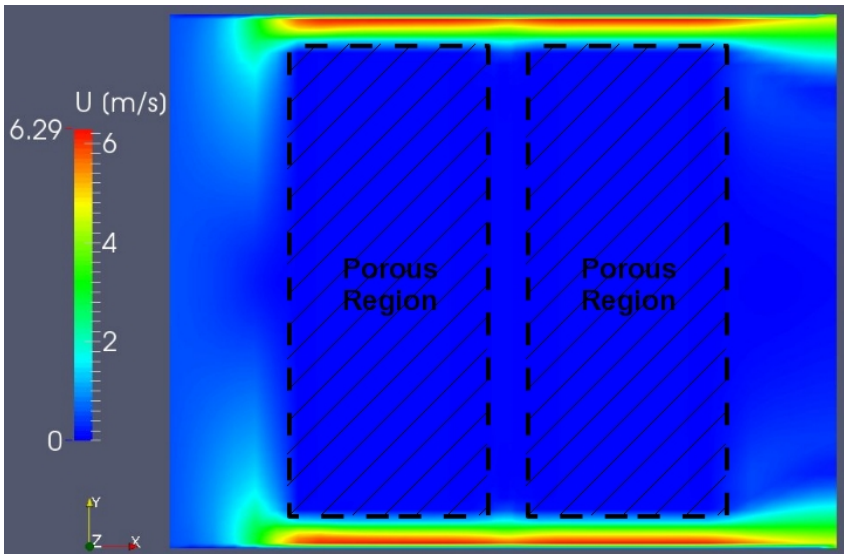

Figure 3.12: Velocity field on a thermal tank with two layers of porous medium. The gas flows in the positive x direction.

where d_p is the particle's diameter and ε the void fraction of the packed bed.

A preliminary test case of a thermal reservoir with two separate porous regions has been prepared using the OpenFOAM solver rhoPorousSimpleFoam and the Darcy-Forchheimer model, assuming estimated values of $d_p = 0.01$ m and $\varepsilon = 0.4$. Figure 3.12 shows the velocity field obtained at steady-state, where it can be seen that most of the gas bypasses the porous regions through the open upper and lower spaces next to the reservoir walls, due to the higher resistance to flow presented by the porous regions. Further steps need to be followed before obtaining useful results from these simulations. First, more porous layers have to be added and valves have to be included in the mesh as to be able to force the gas only through certain layers. Second, the solver will need to be modified as to be able to perform heat transfer calculations with the porous regions. This will allow to closely study the benefits (and disadvantages) of layered packed-bed stores for thermal energy storage and evaluate the impact of using different configurations.

Chapter 4

Final Remarks and Future Work

This final chapter has been divided in three parts. First, a list of the work that has been realized until now is presented in 4.1. Second, the results and conclusions extracted from such work are explained in 4.2. Finally, the activities for future research are discussed in 4.3.

4.1 What has been done so far

The main tasks that have been performed during this year (some of which are still ongoing activities) are summarized below:

- Knowledge has been gained on the several energy storage technologies that have been implemented or proposed so far in the literature, particularly in the field of Thermo-Electrical Energy Storage (TEES).
- The Joule-Brayton (JB) cycle for electricity storage applications has been studied from a thermodynamic perspective. Existing analyses in the literature have been reviewed and extended (see section 2.2).
- This report has proposed new configurations to allow the use of liquid media in the thermal reservoirs (see section 2.3). A summary of liquid materials that are attractive for bulk sensible heat energy storage has been done (see 2.3.1).
- Several adaptations of the Rankine cycle for electricity storage applications (using the steam cycle only during discharge, or using other working fluids such as ammonia or CO_2) have been suggested in the literature. A critical review of such adaptations was done in sections 2.4.1 and 2.4.2.
- The potential of using the steam cycle both as a heat pump and a heat engine for electricity storage was discussed in 2.4.3, where key developments found in the literature

that could enable such use are presented.

- A loss-free model of a reciprocating compressor was built (see section 3.3), and it was used to study the capability of a reciprocating compressor to independently vary the operating pressure ratio and the mass flow rate.
- An existing counter-flow heat exchanger iterative model was extended to account for the fluids' varying thermophysical properties (see 3.2).
- Documentation on the OpenFOAM software was read, and several tutorials were followed in order to learn how to perform Computational Fluid Dynamics (CFD) simulations using it.
- Two OpenFOAM incompressible solvers were modified to perform heat transfer calculations (see 3.4). The modified solvers were used to simulate of flow around a cylinder, and validation of the results was done by comparison with drag and heat transfer correlations from the literature.
- Knowledge on how to use the Darcy-Forchheimer model to describe porous regions in OpenFOAM was gained, which will be used to run CFD simulations of segmented packed-bed thermal reservoirs (see 3.5).

4.2 Conclusions from what has been learned

The main remarks that can be extracted from what has been learned during this first year are presented below:

- TEES systems are based on the idea of combining a heat pump and a heat engine to store electricity in the form of thermal energy. Even though the ideal round-trip efficiency of such a process is one, several irreversible processes that occur in reality diminish the final performance. From what has been learned by reviewing the literature, TEES systems are characterized by having high energy densities (comparable to those of electrochemical batteries), they have no geographic constraints and primarily use environmentally friendly materials.
- A TEES system which is based on the JB cycle and is known as Pumped Thermal Electricity Storage (PTES) has received attention by various research groups. While research activities in the literature have focused until now on a PTES scheme that uses solid media for sensible heat storage, this report has shown that it is also possible to

use liquid media, which would be particularly advantageous for applications that require extended storage periods. While a constraint on the use of liquid media is the more restricted temperature range at which they can be operated, different strategies have been considered to overcome this limitation (see section 2.3). It has been found that the most promising strategy is the use of an additional gas-gas heat exchanger (recuperator) in between the hot and the cold parts of the cycle.

- Several other TEES systems have been suggested in the literature which are based on variations of the Rankine cycle. One advantage of the Rankine cycle, when compared to the JB cycle, is its increased work ratio. On the other hand, storing energy separately in the form of sensible heat and latent heat becomes necessary to minimize irreversible heat transfer. It has been found that a range of working fluids are possible, and careful matching between the condensation/evaporation points of each fluid and the Phase Change Materials (PCM) used for latent heat storage is essential. Additionally, some working fluids present large variations of their heat capacities, causing pinch-point problems in the heat exchangers. More research in this area is necessary to identify and match the most suitable working fluids and energy storage media.

- In order to be able to produce accurate calculations of a full thermodynamic cycle, it is necessary to have adequate sub-models of each component of the cycle. For this purpose, the development of a heat exchanger model and a reciprocating compressor model has been started (see chapter 3), and further work is detailed in the next section.

- The loss-free model of a reciprocating compressor has shown the capability of the device to independently control the pressure ratio and the mass flow rate by means of varying the timings of the valves. Nevertheless, further development of the model is necessary to assess the impact of such variation on the nominal performance of the device.

- The inclusion of varying thermophysical properties on an iterative model of a counter-flow heat exchanger has uncovered pinch-point problems that appear when the specific heat capacity of one of the fluids varies substantially between inlet and outlet. Therefore, the inclusion of such a model is necessary to accurately analyse cycles that involve transfer of sensible heat via heat exchangers with large temperature differences between ends.

4.3 Future work

The following two general goals have been set:

1. Comparison between solid and liquid sensible heat storage methods, and latent heat storage methods, from an exergetic point of view, including the periods of charge, storage and discharge.

2. Development of component models and cycle models that enable the comparison between different Thermo-Electrical Energy Storage systems and the proposal of new, optimized configurations.

In order to accomplish these goals, the following activities will be performed:

- **Heat exchanger modelling**. An iterative code to compute the temperature and heat transfer distribution along a counter-flow heat exchanger was extended to account for the fluids' varying thermophysical properties (see section 3.2). The model will be further developed to include geometrical parameters that permit the calculation of the Reynolds number, friction coefficient and heat transfer coefficient at each section of the heat exchanger. This will allow the computation of important parameters such as the effectiveness and the pressure drop for different geometries (i.e. concentric tube, compact plate type, etc.) under different operating conditions, and therefore to study how to minimize the exergetic losses associated with sensible heat storage using liquid media. Additionally, once the model is ready, it will be adapted to study the Screw Heat Exchanger for latent heat storage described in section 2.4.3. The two versions of the model obtained (one for sensible heat, the other for latent heat) will be used as components for full cycle modelling.

- **CFD of packed-bed thermal reservoir**s. Segmentation of the thermal reservoirs in several layers has been suggested as a way to reduce the overall pressure loss and enable the use of smaller particles, which reduces the spread of the thermal gradient and increases the utilization of the reservoir [53]. Nevertheless, the magnitude of the losses associated with the valve mechanism is not yet clear. This aspect will be investigated by means of CFD simulation, as discussed in section 3.5, together with other effects of interest like heat transfer between layers during the storage period (through convection and radiation) that need to be assessed. Packed-beds of particles can be simulated in OpenFOAM using the Darcy-Forchheimer model of porous media. Nevertheless, the current implementation in the standard OpenFOAM solvers like rhoPorousSimpleFoam is limited as it only includes a pressure sink in the momentum equation of

the gas in the regions of porous media, but does not stablish a separate energy equation of the solid media that enables heat transfer calculations between gas and solid. Therefore, a new solver that includes the properties of the solid and its energy equation will have to be developed. A tutorial from C. Soulaine exists which shows how to develop an OpenFOAM solver for heat transfer calculations in porous media [56]. Unfortunately, the solver seems to strictly simulate porous media and not treat other gas-only regions that are of our interest when studying segmented thermal reservoirs. Still, it will provide useful tools towards implementing porous heat transfer in the standard solvers. Finally, an adequate selection of drag coefficient and heat transfer coefficient correlations for packed-beds will be used to characterise the porous media. Correlations will be gathered from the literature and compared to CFD simulations of packed-bed particles, continuing the work described in section 3.4. While at this stage two-dimensional simulations of flow and heat transfer around one single particle have been performed, these will have to be extended to three dimensions and various particles, using unstructured grid tools like snappyHexMesh.

- **Model of a reciprocating compressor**. The model developed in section 3.3 has to be expanded to account for the different loss mechanisms that affect the device's performance, and be able to predict how these change under different operating conditions. A member of our research group, Dr. Willich, is currently performing CFD simulations to study in detail these loss mechanisms, and the model described in 3.3 was built together with her. The aim is to use the results from her CFD simulations to characterize the loss parameters for the compressor model. After validation by comparison with the results of other models of reciprocating devices described in the literature, it will be used as a component for full cycle analysis.

- **Working fluids, sensible heat storage materials and phase-change materials screening and matching**. As described in the previous section and in section 2.4, variations of the Rankine cycle for electricity storage require a good matching between the working fluid used to drive the cycle and the materials used for sensible and latent heat storage. Particularly important is the matching between the condensation/evaporation temperature of the working fluid, at an adequate pressure level, with the phase-change temperature of the Phase Change Materials (PCM). Therefore, a systematic screening, evaluation and matching of working fluids and TES materials is necessary. A review of potentially attractive liquids for sensible energy storage was performed for this report and was presented in section 2.3.1. For latent heat storage materials, reviews of high-temperature PCMs like the one by Kenisarin in [57] will be used. For selecting and evaluating several common working fluids, the CoolProp library of thermophysical

properties will be employed. Candidate working fluids will be able to achieve condensation/evaporation points at adequate pressure levels and will exhibit small variations of their specific heat capacities over the selected temperature ranges. The working fluids and the selected liquids for sensible heat storage will be tested together using the counter-flow heat exchanger model to identify and assess possible pinch point problems. The most promising materials will be used for the full cycle analysis.

- **Cycle modelling and cycle comparison**. The final stage of the project will involve gathering the results from the research activities that have been discussed in this chapter to develop two full cycle models: one for the Joule-Brayton cycle and one for the variations of the Rankine cycle. The models will serve to compare different performance parameters and propose novel, optimized configurations.

The proposed schedule for the research activities above is shown in Figure 4.1.

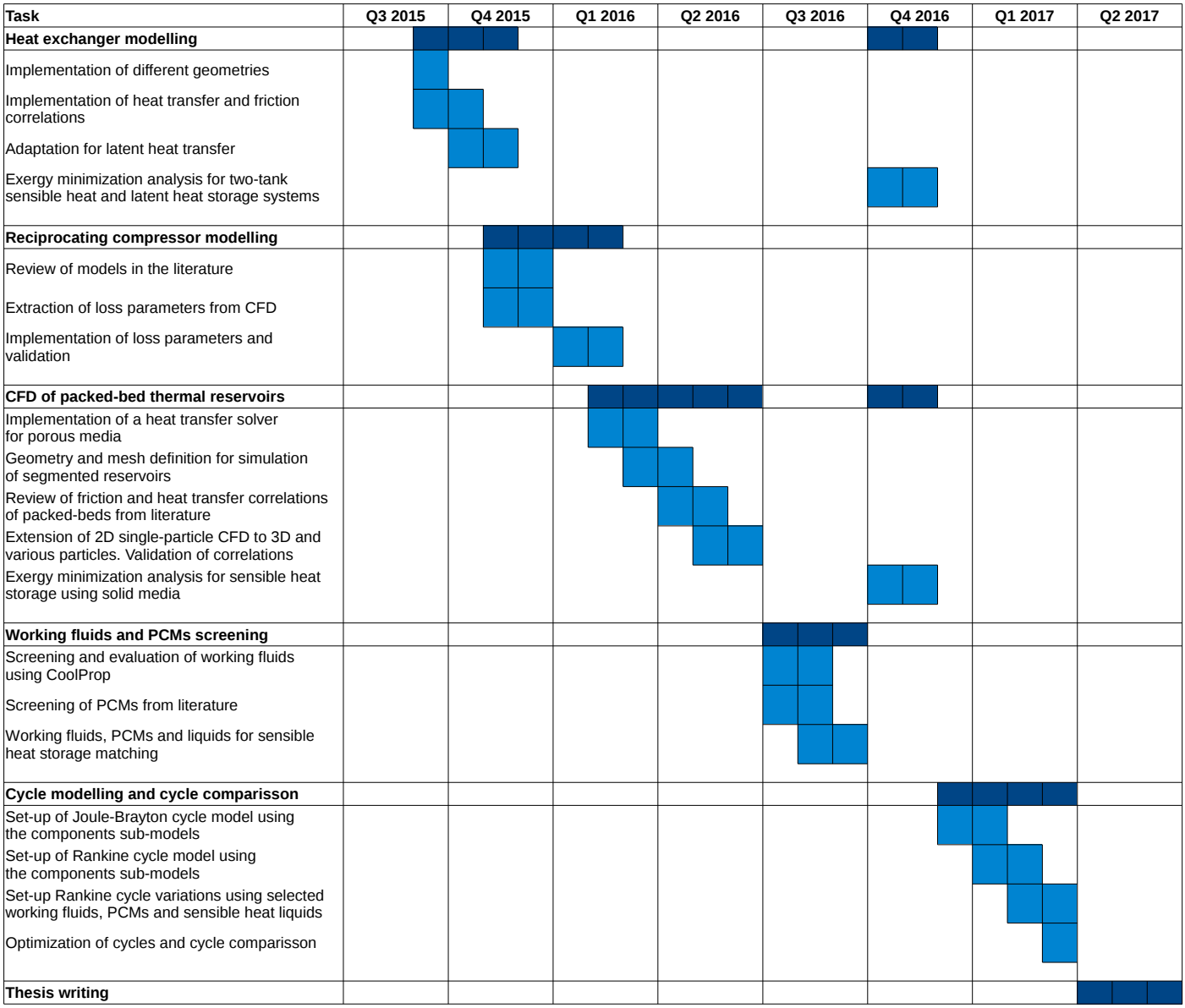

Figure 4.1: Gantt chart of planned research activities.

Acknowledgements

The author of this report gratefully acknowledges the graduate studentship that Peterhouse awarded to him, thanks to which he is being able to pursue this research project at Cambridge University Engineering Department.

References

[1] European Parliament. Directive 2009/28/EC of the European Parliament and of the Council of 23 April 2009. *Official Journal of the European Union*, 140(16):16–62, 2009.

[2] International Energy Agency. Prospects for Large-Scale Energy Storage in Decarbonised Power Grids. 2009.

[3] D.J.C. MacKay. *Sustainable Energy - without the hot air*. UIT Cambridge, 2008. Available free online from www.withouthotair.com.

[4] I.A.G. Wilson, P.G. McGregor, and P.J. Hall. Energy storage in the UK electrical network: Estimation of the scale and review of technology options. *Energy Policy*, 38(8):4099–4106, 2010.

[5] H. Chen, T.N. Cong, W. Yang, C. Tan, Y. Li, and Y. Ding. Progress in electrical energy storage system: A critical review. *Progress in Natural Science*, 19(3):291–312, 2009.

[6] X. Luo, J. Wang, M. Dooner, and J. Clarke. Overview of current development in electrical energy storage technologies and the application potential in power system operation. *Applied Energy*, 137:511–536, 2015.

[7] C. Bullough, C. Gatzen, C. Jakiel, M. Koller, A. Nowi, and S. Zunft. Advanced Adiabatic Compressed Air Energy Storage for the Integration of Wind Energy. *Proceedings of the European Wind Energy Conference*, (November):22–25, 2004.

[8] Y.M. Kim, D.G. Shin, S.Y. Lee, and D. Favrat. Isothermal transcritical CO2 cycles with TES (thermal energy storage) for electricity storage. *Energy*, 49:484–501, 2012.

[9] Samuel Henchoz, Florian Buchter, Daniel Favrat, Matteo Morandin, and Mehmet Mercangöz. Thermoeconomic analysis of a solar enhanced energy storage concept based on thermodynamic cycles. *Energy*, 45(1):358–365, 2012.

[10] A.J. White. Thermodynamic analysis of the reverse Joule-Brayton cycle heat pump for domestic heating. *Applied Energy*, 86(11):2443–2450, 2009.

[11] A.J. White, G. Parks, and C. Markides. Thermodynamic analysis of pumped thermal electricity storage. *Applied Thermal Engineering*, 53(2):291–298, 2013.

[12] T. Desrues, J. Ruer, P. Marty, and J. F. Fourmigué. A thermal energy storage process for large scale electric applications. *Applied Thermal Engineering*, 30(5):425–432, 2010.

[13] A.J. White. Thermal Energy Storage Systems (and Devices) for Electrical Energy Applications. In *UK Thermal Energy Storage Workshop 2015*, Birmingham, 2015.

[14] J. Ruer. Installation et procedes de stockage et restitution d'energie electrique. Patent No. WO 2008/148962 A2, 2007.

[15] J. Macnaghten and J.S. Howes. Energy storage. Patent No. WO 2009/044139 A2, 2007.

[16] A.J. White. Loss analysis of thermal reservoirs for electrical energy storage schemes. *Applied Energy*, 88(11):4150–4159, 2011.

[17] A.J. White, J. McTigue, and C. Markides. Wave propagation and thermodynamic losses in packed-bed thermal reservoirs for energy storage. *Applied Energy*, 130:648–657, 2014.

[18] J. McTigue, A.J. White, and C. Markides. Parametric studies and optimisation of pumped thermal electricity storage. *Applied Energy*, 137:800–811, 2015.

[19] J. Howes. Concept and development of a pumped heat electricity storage device. *Proceedings of the IEEE*, 100(2):493–503, 2012.

[20] Hall Dixon. *Fluid Mechanics and Thermodynamics of Turbomachinery (6th Edition)*. Elsevier, November 2010.

[21] W.D. Steinmann. Thermal energy storage systems for concentrating solar power (CSP) technology. In *Advances in Thermal Energy Storage Systems*, chapter 21, pages 511–531. Elsevier Ltd. Knovel, 2015.

[22] E.W. Lemmon, M.O. McLinden, and D.G. Friend. *Thermophysical Properties of Fluid Systems*. NIST Chemistry WebBook, NIST Standard Reference Database Number 69, Eds. P.J. Linstrom and W.G. Mallard, National Institute of Standards and Technology, Gaithersburg MD, 20899. http://webbook.nist.gov.

[23] J. C. O. Santos, M. G. O. Santos, J. P. Dantas, Marta M. Conceição, P. F. Athaide-Filho, and a. G. Souza. Comparative study of specific heat capacities of some vegetable oils obtained by DSC and microwave oven. *Journal of Thermal Analysis and Calorimetry*, 79(2):283–287, 2005.

[24] Michael Bockisch. *Fats and Oils Handbook*. AOCS Press, March 1998.

[25] Irina Nita, Anisoara Neagu, Sibel Geacai, Anca Dumitru, and Anca Sterpu. Study of the behavior of some vegetable oils during the thermal treatment. *Ovidius University Annals of Chemistry*, 21(1):5–8, 2010.

[26] Coastal Chemical Company. HITEC Heat Transfer Salt. Technical report, Houston.

[27] C.L. Yaws. *Yaws' Transport Properties of Chemicals and Hydrocarbons (Electronic Edition)*. Knovel, 2010.

[28] CHERIC (Chemical Engineering Research Information Center). Korean Thermophysical Properties Data Bank. http://www.cheric.org/research/kdb/.

[29] S. Ushak, A.G. Fernandez, and M. Grageda. Using molten salts and other liquid sensible storage media in thermal energy storage (TES) systems. In *Advances in Thermal Energy Storage Systems*, chapter 3, pages 49–63. Elsevier Ltd. Knovel, 2015.

[30] Thomas Bauer, Nicole Pfleger, Nils Breidenbach, Markus Eck, Doerte Laing, and Stefanie Kaesche. Material aspects of Solar Salt for sensible heat storage. *Applied Energy*, 111:1114–1119, 2013.

[31] R. Serrano-López, J. Fradera, and S. Cuesta-López. Molten salts database for energy applications. *Chemical Engineering and Processing*, 73:87–102, 2013.

[32] C.L. Yaws. *Yaws' Handbook of Thermodynamic and Physical Properties of Chemical Compounds*. Knovel, 2003.

[33] Michael E Van Valkenburg, Robert L. Vaughn, Margaret Williams, and John S. Wilkes. Thermochemistry of ionic liquid heat-transfer fluids. *Thermochimica Acta*, 425(1-2):181–188, 2005.

[34] Halotechnics Inc. High Temperature Thermal Fluids. In: www.halotechnics.com. Accessed: July 2015.

[35] C.L. Yaws. *Yaws' Handbook of Properties of the Chemical Elements*. Knovel, 2011.

[36] Heat Transfer International. Ceramic Heat Exchangers. Technical report, Kentwood, MI.

[37] N.P. Padture, M. Gell, and E.H. Jordan. Thermal Barrier Coatings for Gas-Turbine Engine Applications. *Science*, 296(April):280–284, 2002.

[38] R.J. Miller. Thermodynamics - Lecture Notes. CUED Part IB Paper 4., 2013.

[39] Halotechnics Inc. Grid Scale Electricity Storage. In: www.halotechnics.com. Accessed: August 2015.

[40] Y. Hong and G. Xin-shi. Preparation of polyethylene-paraffin compound as a form-stable solid-liquid phase change material. *Solar Energy Materials and Solar Cells*, 64(1):37–44, September 2000.

[41] Ming Liu, Wasim Saman, and Frank Bruno. Review on storage materials and thermal performance enhancement techniques for high temperature phase change thermal storage systems. *Renewable and Sustainable Energy Reviews*, 16(4):2118–2132, 2012.

[42] V. Zipf, A. Neuhäuser, D. Willert, P. Nitz, S. Gschwander, and W. Platzer. High temperature latent heat storage with a screw heat exchanger: Design of prototype. *Applied Energy*, 109:462–469, 2013.

[43] F.P. Incropera, D.P. DeWitt, T.L. Bergman, and A.S. Lavine. *Fundamentals of Heat and Mass Transfer*. John Wiley and Sons, 6th edition, 2007.

[44] P.S. Ghoshdastidar. *Heat Transfer (2nd Edition)*. Oxford University Press, May 2012.

[45] I.H. Bell, J. Wronski, S. Quoilin, and V. Lemort. Pure and pseudo-pure fluid thermophysical property evaluation and the open-source thermophysical property library coolprop. *Industrial and Engineering Chemistry Research*, 53(6):2498–2508, 2014.

[46] R. Anderson, S. Shiri, H. Bindra, and J.F. Morris. Experimental results and modeling of energy storage and recovery in a packed bed of alumina particles. *Applied Energy*, 119:521–529, 2014.

[47] OpenFOAM Foundation. *OpenFOAM. The Open Source CFD Toolbox. User Guide (Version 2.3.0)*. www.openfoam.org, 2014.

[48] B.S. Massey and J. Ward-Smith. *Mechanics of fluids*. Stanley Thornes, Cheltenham, 7th edition, 1998.

[49] D.J. Tritton. *Physical Fluid Dynamics*. Clarendon, Oxford, 2nd edition, 1988.

[50] OpenFOAMwiki.net. How to add temperature to icoFoam, 2014.

[51] S. Sanitjai and R.J. Goldstein. Forced convection heat transfer from a circular cylinder in crossflow to air and liquids. *International Journal of Heat and Mass Transfer*, 47:4795–4805, 2004.

[52] E.M. Sparrow, J.P. Abraham, and J.C.K. Tong. Archival correlations for average heat transfer coefficients for non-circular and circular cylinders and for spheres in cross-flow. *International Journal of Heat and Mass Transfer*, 47:5285–5296, 2004.

[53] J.D. Mctigue and A.J. White. Segmented Packed Beds for Improved Thermal Energy Storage Performace. In *OSES - Offshore Energy & Storage Symposium*, 2015.

[54] H.E. Hafsteinsson. Porous Media in OpenFOAM. Technical report, Chalmers University of Technology, Gothenburg, 2009.

[55] A. Bejan. Convection in porous media. In *Convection Heat Transfer*, chapter 12, pages 537–605. John Wiley & Sons, Inc., 4th edition, 2013.

[56] C. Soulaine. Introduction to fluid mechanics simulation using the OpenFOAM technology. Simulation in porous media from pore to large scale. *Stanford University. School of Earth Sciences*, 2014.

[57] M.M. Kenisarin. High-temperature phase change materials for thermal energy storage. *Renewable and Sustainable Energy Reviews*, 14(3):955–970, 2010.